NOZZLE FLOW STUDY AND GEOMETRY OPTIMIZATION OF SHEAR THINNING NON-NEWTONIAN FLUID, FUEL TANK SEALANT

A THESIS

Presented to the Department of Mechanical and Aerospace Engineering

California State University, Long Beach

In Partial Fulfillment

of the Requirements for the Degree

Master of Science in Mechanical Engineering

Committee Members:

Mahdi Yoozbashizadeh, Ph.D. (Chair)
Hamid Rahai, Ph.D. (Co-Chair)
Parviz Yavari, Ph.D.

College Designee:

Antonella Sciortino, Ph.D.

By Niloufar Kiani

B.S., 2010, Isfahan University of Technology (IUT), Iran

August 2018

ABSTRACT

NOZZLE FLOW STUDY AND GEOMETRY OPTIMIZATION OF SHEAR THINNING NON-NEWTONIAN FLUID, FUEL TANK SEALANT

By

Niloufar Kiani

August 2018

Applications of sealant and adhesive technologies in aerospace industries require appropriate and reliable sealing materials and tools to provide suitable sealing. Due to a growing use of integral fuel tanks, which utilize the aircraft structure for fuel containment, this study focuses on nozzle geometry optimization of aircraft fuel tank sealant in order to develop and facilitate sealant approval process and to ensure the implementation of suitable fuel tank sealing.

Computational Fluid Dynamics (CFD) analyses were performed to study the sealant flow characterization and behavior using Star-CCM+ software. An empirical model was developed by the aid of Design of Experiments (DOE) techniques in order to develop a reliable mathematical model based on the collected data from numerical results. Scanning Electron Microscopy (SEM) was utilized to investigate the fracture/deformation of hollow glass microballoons and entrapped air bubbles within the cured sealant.

The results of this research concluded that the bent angle in nozzle geometry increases the sealant pressure drop throughout the nozzle. There is an optimized value for travel distance and cross sectional dimension and geometrical shape within the nozzle geometry that minimizes overall dynamic viscosity of the sealant.

ACKNOWLEDGMENTS

First I would like to sincerely thank my thesis advisor Dr. Mahdi Yoozbashizadeh for his technical support and encouragement. He led me through the right path whenever needed during this study. I would like to thank Dr. Hamid Rahai for his deep insight and unlimited support for this study, as well as, Dr. Parviz Yavari for his valuable guidance and contribute to this study. I also would like to express my gratitude to my lovely family and my loved husband for their unconditional love and support.

TABLE OF CONTENTS

LIST OF TABLES

LIST OF FIGURES

LIST OF ABBREVIATIONS

CFD	Computational Fluid Dynamics
DOE	Design of Experiments
RSM	Response Surface Methodology
SEM	Scanning Electron Microscopy

CHAPTER 1

INTRODUCTION

Sealant and adhesive technologies are essential to many industries such as automotive, aerospace, flexible packaging, assembling, and general manufacturing. Further, adhesive and sealant technologies play a key role in numerous industries to improve the automation and modernization [1]. For example in the automotive industry, the Original Equipment Manufacturers (OEM) use adhesives and sealants instead of welding and mechanical rivets to attach metallic substrates. In this way they simplify their manufacturing process and decrease their manufacturing costs substantially [1].

According to a recent market report by MarketsandMarkets research team, it is estimated that the automotive adhesives market will grow from US$4.03 billion in 2016 to US$6.05 billion by 2021 at a compound annual growth rate of 8.5% [2]. In addition to the aforementioned industrial applications of adhesive and sealing technologies, the medical and dental industry is another beneficiary of sealant and adhesive technologies. Medical applications sometimes face even more challenges and threats compared to other industries; for instance, seal failure can insert too large or too small of a dose of a drug into a patient, or it can cause harmful reactions in seal materials of the artificial organs [3]. Moreover, sealant home usage can be considered the most common application of sealant and adhesive industry, including sealing in bathrooms, kitchens, and windows.

The aerospace industry emerged through a series of innovations, and most probably remains an attractive area for researchers, scientists, and engineers to overcome the exciting challenges. In the manufacturing process of aircrafts, attaching any parts together requires different tools and mechanisms. For instance, in modern aircraft design the fuel tank is

considered a major part of the actual structure of the aircraft and is most frequently located in the wings in commercial aircrafts and contains large amounts of jet fuel. In military aircraft, in addition to the wings, irregular shaped cavities inside the fuselage are also used to convey the fuel. This kind of fuel tank, called an integral fuel tank, has advantages over old fashioned rigid removable and bladder fuel tanks; such advantages include higher capacity and, since it is itself a part of the main structure, there is not any extra weight to the aircraft [4].

Along with these benefits, utilizing the integral fuel tank has its own requirements. It requires appropriate, reliable, and long service life sealing material to be able to provide suitable sealing in the wing's structure. Applications of this technique in the wing's structure can be used between assembled faces, for filleting, and for over coating. In addition, suitable sealing prevents the expenditure of extra costs for reinjection, leakage in inaccessible areas, and external objects entering the fuel tank. Moreover, the quality of the sealant material should be competitive with the various environmental situations such as harsh temperatures, imposed load, and direct connection with fuel from inside and water from outside [4, 5]. Although mechanical and physical testing are considered to determine the characteristics of the sealant material and ensure that it is perfectly fit for its sealing job, finding the appropriate dispensing equipment and most efficient methods for applying the sealant materials are important factors that should be taken into account. Technically, it is recommended to carry out a complete task analysis by considering all the factors that influence the applying equipment [6].

There are three different categories of dispensing process: manual dispensing, semi-automatic dispensing, and robotic or fully automatic dispensing. Based on the situation and technical requirements, the manufacturer will pick out the proper method for dispensing the sealant. This thesis employs the manual dispensing method. In manual dispensing, the operators

have controls on the flow rate and volume dispensed. The usual equipment for this process is a cartridge, caulking gun, and various types of nozzles [6].

In regard to sealants' properties as a non-Newtonian fluid with shear thinning behavior, there are some concerns about process equipment when applying sealant to the purpose area. Non-Newtonian flows in general are more complex, and it is more difficult for them to flow through the tubes or any processing equipment than it is for Newtonian flows. Because of this, there are studies that have been done on how to facilitate their flowing process. For example, Barnes et al. [7] worked on how the volumetric flow rate (per time-average) of a non-Newtonian fluid (polymer solution) increased based on pulsating pressure gradient in the axis direction. Hyun et al. mentioned in their paper [8] that design of fluidic systems, which deal with shear thinning non-Newtonian fluid, have significant problems specifically related to wall shear stress. The wall shear stress has direct effects on the apparent viscosity of the non-Newtonian fluid. For example, increasing the value of wall shear stress leads to flow tumbling and vorticity in the blood cell [8].

Another study is done by the Air Force Material Library [4]; this study confirmed that lower obtainable levels of fuel tank sealant viscosity throughout the nozzle have influence on the mass flow inlet, pressure, and shear-flow behavior. The study showed that the duration of a process relates to the mass flow inlet and consequently to the pressure distribution pattern. Generally, the duration of the process is important in industries, and reduced duration is often viewed as a sign of perfect work. Another point mentioned in the report is about pressure differential throughout the nozzle, which is higher when the sealant viscosity is higher [4].

By going through more specific details about aircraft fuel tank sealant material and its application process, some common and considerable difficulties for sealant in the nozzle will be detected. This study focuses on several such difficulties, which are as follows:

Internal flow transition from laminar to turbulent regime: This crucial change is sensitive to the nozzle geometry [9]. The flow inside the nozzle should be kept laminar during the process by considering the duct Reynolds number or considering the critical Reynolds number when there are irregularly shaped ducts, such as the nozzles in our study. If any clue of transition regime occurs, it means that there is distribution between layers of the flow and the internal flow streamlines are not parallel anymore; as a result, an inconstant flow rate and high pressure drop from inlet to outlet of nozzle will be experienced, and more exerted back pressure will be required in order to make the sealant flow inside the nozzle.

Appearance of stagnation points in the flow inside the nozzle: Stagnation points may appear in the vicinity of any internal duct blade or any sudden cross section changes; when stagnation points do appear, the velocity of the flow decreases almost to zero, also the distribution in internal flow happens that leads to appearing characters of the turbulent flow such as eddies and vortices.

Clogging occurs inside the nozzle: This clogging is caused by sudden geometry changes inside the nozzle, and also by stagnation points.

Curing of sealant happens inside the nozzle: If the sealant starts curing inside the nozzle, the flow rate will decrease and the flow motions become slightly violent; further, it can cause significant maintenance issues for the nozzle, the flow may be totally choked inside the nozzle if the curing happens on a large scale.

Crushing of hollow glass microballoons: Hollow microballoons have prevalent industrial use, generally as additives or fillers in a wide range of products such as sealants, epoxies, pipe insulation, and thermoplastic resins. The advantages of hollow glass microballoons within the sealant include, but are not limited to, weight reduction, impact strength improvement, increases to volume load capacity, and improvement to thermal insulation [10]. The hollow glass microballoons are at risk of rupturing and breakage under high shear rate conditions and high surrounding pressure.

Generation of air bubbles inside the sealant material: The air bubbles inside the sealant make the sealant permeable and also decrease the strength of the material in their vicinity; in addition, more back pressure is required to keep the sealant flow inside the nozzle. When the sealant flows inside the nozzle, air bubbles can be generated inside the sealant due to the existence of stagnation points, generation of vortexes, or production of turbulence in the more severe cases. This phenomenon can be caused by abrupt changes of cross section, sharp changes of direction, or the existence of an intense irregular internal geometric inside the nozzle. Thus, another important task is trying to avoid generating air bubbles inside the sealant material and mitigation of the air bubbles trapped inside the sealant material.

In fluidic systems that deal with non-Newtonian fluids, internal geometry configurations have significant effects on the flow rate, flow ability, and durability of the internal flow. The overall performance of the system is significantly affected by both external geometric patterns and internal geometry configurations. For example, Payri et al. [11] worked on the effect of nozzle geometry on internal flow and spray characterization. As it was presented in their study, the design approximation method can be divided into two classes. The first follows the elementary method of trial and error; that is, it involves a repetitive loop that produces and

performs until the system's criteria are satisfied. This method obviously wastes time and materials and is not economical at all. The second one is by aid of Computational Fluid Dynamic analysis and Design of Experiment techniques for data collection and optimization. Clearly the second method has better economic and technical benefits [8]. The second class of approach will be used as the approaching methodology in this study.

There is a range of aircraft sealants suitable for use in different parts of aircraft structures, such as for sealing the fuel tank, sealing aircraft windshields, and protecting aircraft mating surface. Aerospace industries have been working diligently to improve the quality and durability of aircraft sealant materials, making them environmentally friendly, and producing rapid cure light weight/low density sealant. The improvements have included simplifying the sealant application process by producing complete suitable packages of sealant application including cartridges, nozzles, caulking guns, and mixing machines for non-premixed material.

The PPG Aerospace is a well-known company in providing unique groups of products and services in aerospace industries. Among their many different products, they also have various kinds of nozzles for sealant application [12]. In this study, several PPG Semco nozzles with distinctive features have been selected. These nozzles will be used to investigate the effect of geometrical features on the dynamic viscosity behavior and pressure drop of the sealant throughout the nozzle. This study will be conducted by a special type of fuel tank sealant, PR-1776M Class-B, to study the flow through the nozzles.

Using the aforementioned explanations about non-Newtonian fluids' properties and geometry optimization of the fluidic system dealing with these fluids, the finding of this research will propose optimum geometrical features to minimize the pressure drop and the overall dynamic viscosity of the sealant. The complete explanation on the Navier-Stokes equations

governing the internal sealant flow inside the nozzle, on the boundary conditions considered for the selected nozzle geometries, and on the generalized Newtonian Carreau-Yasuda model that is used to model the shear thinning non-Newtonian sealant behavior, will be provided in the following chapters.

Computational Fluid Dynamics (CFD) is a strong tool to investigate the flow characterization and numerical solution analysis. In this study, Star-CCM+ software will be used to simulate the experimental settings. Design of Experiments techniques, using Surface Response Methodology, will be used for data collection and analysis of the data. An optimum model for the sealant nozzle applicator will be identified by using various optimization techniques.

The next step is validating the CFD simulations and verifying our presented model with experimental data. All the required equipment for practical experiments of this study is purchased from PPG Aerospace company; furthermore, a nozzle with the optimized geometry will be modeled and 3D printed to be used as our optimum module in practical experiments. By attaching a handheld digital manometer to the module and a mechanized caulk gun, which moves at a constant speed, a system to measure the static pressure drop from inlet to outlet of the module will be provided. More explanation on this is presented in chapter 5, which provides complete explanations and details of practical experiments procedure.

In addition, the experimental study will be conducted on mitigating the air bubbles and breaking the hollow glass microballoons inside the sealant material. For scanning the small size air bubbles inside the sealant after curing, the nozzle will be sliced longitudinally and the existing air bubbles will be measured in the cross sectional areas. The amount of air bubbles per cross section area will be calculated and used as the indicator of air bubble formation, air bubble entrapment, and air bubble mitigation. In addition, to investigate the effects of different pressures

and shear rate conditions on the rupturing of hollow glass microballoons, an experimental study will be carried out utilizing SEM (Scanning Electron Microscope) imaging method. This will be fully discussed in chapter 5.

In chapter 2, the review of literature for governing equations on non-Newtonian fluid model, the appropriate physic models, and the boundary conditions for our fluidic system design will be provided. Chapter 3, which demonstrates the modeling of the nozzles in SolidWorks software in addition to CFD simulation setups with Star-CCM+ software, also explains and presents the numerical analysis theory and simulation data results. Chapter 4 presents the Response Surface Methodology, using Design of Experiments (DOE) techniques, for data collection, data analysis, and optimization of the nozzle geometry. In chapter 5, experimental settings for validating the CFD simulations will be presented. Finally in chapter 6, conclusion and future works will be presented.

CHAPTER 2

REVIEW OF LITERATURE

2.1 History

As discussed earlier, this study focuses on nozzle geometry optimization and nozzle flow study of non-Newtonian shear thinning fuel tank sealant. Although much research has been done on geometry optimization, topology, and shape optimization for fluidic systems, a few research projects have focused on nozzles and fluidic systems dealing with non-Newtonian shear thinning fluid; furthermore, no existing research has directly studied nozzle geometry optimization of non-Newtonian shear thinning fuel tank sealant.

Most of the optimal designs of the fluidic systems are generally classified as the shape optimization design. The shape optimization design in fluid mechanics has broad and significant applications in aerodynamic and hydrodynamic topics, such as the design of airplane wings and jet engines' inlet shape. Shape optimization design is usually restricted to identify the optimum shape of an existing boundary [13].

Topology optimization was initially developed for mechanical design problems, but recently this method has been extended into fluidic system applications and design. The topology optimization design can be utilized to design features in the domain, thereby allowing new boundaries to be presented in the design [13]. For example, Borrvall and Peterson [14] carried out the relax material distribution method in order to minimize the power dissipated in creeping flow of Newtonian fluid. They considered the surface material phase as an impermeable phase to be able to approximate the no-slip condition along the solid-fluid interface. They utilized the generalized Stokes problem to model the fluid flow within the domain. Later, Guest and Prévost

built on that study by treating the material phase as a porous medium where the fluid flow is governed by Darcy's law [15].

Payri et al. [11] published a valuable study about the relation between nozzle geometry, internal flow, and the spray characteristics in diesel fuel injection systems. They carried out their study on two bio-orifice nozzles, one cylindrical and one conical. Based on their conclusion, cavitation takes place in the nozzle with lower levels of conicity and a smaller rounding radius. In addition, when cavitation occurs, it causes considerable increases in the spray cone angle.

In another study, Nguyen et al. [16] performed geometry optimization design for several types of magnetorheological (MR) valves, constrained in a specific volume, in order to improve the valve's performance. The objective function in that study was valve ratio, which is defined as the ratio of the viscous pressure drop to the field-dependent pressure drop of the MR valves. The optimal geometrical dimensions of the flow ducts and coils were investigated to obtain the minimum valve ratio. By minimizing this ratio, the performance of the valve, measured by factors such as the field-dependent pressure drop, improves significantly. ANSYS optimization tool and finite element method were used in the aforementioned study.

The recent studies by Pingen and Maute [17] and Hyun et al. [8] on topology optimization design of non-Newtonian flows, will be cited frequently in this study.

Pingen and Maute [17] presented a material distribution-based topology optimization approach for non-Newtonian fluid. They used the Lattice-Boltzmann method and the Carreau-Yasuda generalized model in order to model the flow. Although they obtained their numerical results for a simple structure dual pipe system, Pingen and Maute illustrated that optimal design for Newtonian and non-Newtonian flows at low Reynolds number has significant differences, such as those in pressure and velocity. For instance, velocity of non-Newtonian is larger near the

boundaries in order to increase the boundary velocity gradient and decrease the viscosity. Further, the pressure drop in non-Newtonian flow is larger than the pressure drop in Newtonian flow because of increased non-Newtonian viscosity.

Hyun et al. [8] utilized the topology optimization approach to minimize the wall shear stress for the design of the fluidic system dealing with shear thinning non-Newtonian fluid. In their topology optimization approach, the material interpolation functions for inverse permeability and dynamic viscosity were used; in addition, they defined the wall shear stress on the implicit solid-fluid interface based on the relaxation method of wall shear stress. Since the generalized Newtonian Carreau-Yasuda model was used to model the non-Newtonian flow, blood, in this research, the specifications and differences between Newtonian and non-Newtonian shear thinning fluid were discussed; afterwards, compatibility of both Newtonian and non-Newtonian shear thinning fluids with the generalized Newtonian power law and with the generalized Newtonian Carreau-Yasuda model were demonstrated via backward facing step method.

Figure 1 illustrates the dynamic viscosity distributions for both fluid types when the inlet velocity is relatively low and when it is relatively high. In addition, the non-Newtonian shear thinning flow in each case modeled with both of the generalized Newtonian power law model, (b) and (e), and the generalized Newtonian Carreau-Yasuda model, (c) and (f).

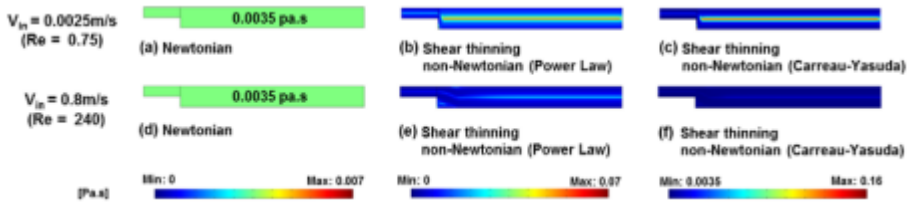

FIGURE 1. Dynamic viscosity distribution of the simple backward-facing step according to inlet velocity and generalized models. Source: Hyun et al. [8].

As it is observed from Figure 1, the Newtonian fluid has constant dynamic viscosity in both cases, (a) and (d). In contrast, the non-Newtonian shear thinning fluid has various dynamic viscosity distributions based on the inlet velocity and generalized Newtonian model applied. In non-Newtonian fluids, the dynamic viscosity reaches into its highest value at the centerline of the channel in furthest distance from the wall, no-slip boundary. The overall non-Newtonian shear thinning dynamic viscosity behavior is almost similar, regardless of the inlet velocity value; however, the dynamic viscosity value at the centerline is relatively smaller when the inlet velocity is slower.

Figure 2 illustrates the velocity profiles for both fluid types when the inlet velocity is relatively low, case (a), and when it is relatively high, case (b). Similar to the previous one, the non-Newtonian shear thinning flow in each case modeled with both the generalized Newtonian power law model, demonstrated by green line, and the generalized Newtonian Carreau-Yasuda model, demonstrated by blue line.

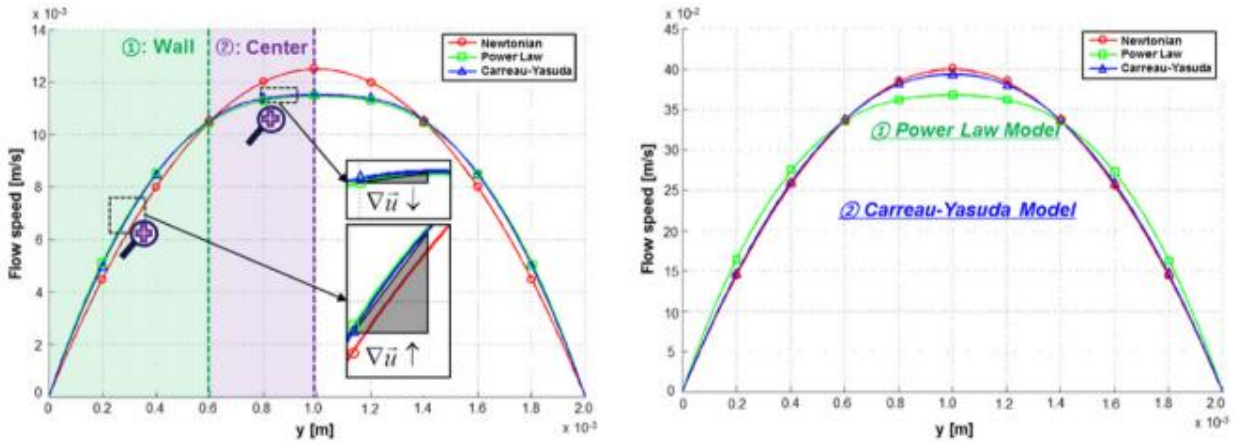

FIGURE 2. Velocity profiles of the simple backward-facing step for the cross-section line according to inlet velocity. Source: Hyun et al. [8].

For the case (a), the Newtonian fluid and shear thinning non-Newtonian fluid behave differently. The velocity profile slope is larger for the shear thinning non-Newtonian fluid than

for the Newtonian fluid, close to the wall; however, it is reverse in the channel centerline. Consequently, the non-Newtonian fluid has the smaller dynamic viscosity and larger shear rate close to the wall; however, opposite happens in the channel centerline. For the non-Newtonian shear thinning fluid in case (b), there is significant difference between generalized Newtonian power law model and generalized Newtonian Carreau-Yasuda model. Since in power law model, there is no limitation for dynamic viscosity at the large and at the small scales, the power law diverges from the Newtonian fluid behavior at these situations. The Carreau-Yasuda model shows more reasonable and reliable behavior.

2.2 Nozzles and Fuel Tank Sealant Study History

In 1977, the Air Force material laboratory published a comprehensive report about fundamental thermal, physical, and chemical properties of fuel tank sealants, and how engineering principles applied on them [4]. Further, Giannis et al. demonstrated how the peel angle, the peel rate, and the thickness of fuel tank sealants affect the peel energy and the peel resistance [5, 18].

In this study, a specific kind of fuel tank sealant, PR-1776M Class B Low Weight Fuel Tank Sealant, is used. The PPG Aerospace company, which produces this kind of sealant, published application guide and technical data sheet of this sealant [19]. This sealant is described as the low density and high temperature aircraft integral fuel tank sealant, which has a service temperature range from -65°F (-54°C) to 250°F (121°C) with limited excursions up to 360°F (182°C). This sealant is a two-part manganese dioxide cured Permapol P-5 modified polysulfide that keeps its elastomeric properties perfectly after a long exposure to aircraft fuels include jet fuel and aviation gas. Since the uncured sealant material is low sag and thixotropic paste, it can

be applied simply by using extrusion guns or spatulas. More technical information for PR 1776M class B will be presented in Appendix A.

As mentioned earlier, analysis of nozzle geometry for many different applications have been performed except for the fuel tank sealant nozzle. For example, Payri et al. [11] investigated the relation between nozzle geometry, internal flow, and the spray characteristics in diesel fuel injection systems. In another study, Yin et al. [20] reviewed the gas flow, particle acceleration, and the heat transfer behavior in the cold spray process in a supersonic de-Laval nozzle; plus, they studied the effect of nozzle geometry on the gas flow properties and on the particle velocity. Moreover, the PPG Aerospace produces more than 100 different commercially available application nozzles; the company design and manufacture their application nozzles based on the principles, such as minimizing the chemical waste, improving their productivity, achieving constant quality, and reducing the total cost of application. They made the nozzles of the high density polyethylene in order to increase their durability [12]. A list of Semco specialty application nozzles will be presented in Appendix B.

2.3 Shear Thinning High Viscous non-Newtonian Fluids

The Newton's Law of viscosity, Equation 1, satisfactorily describes the momentum flux of the simple structural liquid, which can be considered incompressible [21].

Newton's Law of Viscosity:

$$\Pi = p\,\delta + \tau = p\,\delta - \mu\dot{\gamma} \qquad (1)$$

Here "π" is the total momentum flux or stress tensor, which is defined when the force transmits from the negative side of the surface. "δ" is the unit tensor, "τ" is the extra stress tensor, "p" is the isotropic pressure, and "γ̇" is the rate-of-strain. "μ" is the viscosity that depends on

temperature, pressure, and concentration; in contrast, it does not depend on the time or any kinematic quantities like rate-of-strain [21].

The complex structure liquid, such as macromolecular fluids and two-phase fluids cannot be described by Equation 1. These fluids, known as non-Newtonian fluids, are classified according to their different viscosity behaviors. Shear thinning or pseudoplastic is the most common type of time independent non-Newtonian fluids. They exhibit Newtonian behavior when the shear rate is very low or very high. Figure 3 shows the shear rate-shear stress plot of these fluids. As it is illustrated, the plot becomes a straight line near the origin and passes through the origin on a linear scale [22].

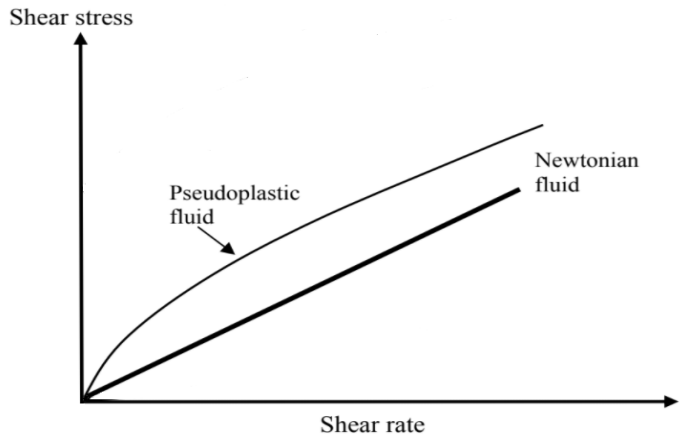

FIGURE 3. Shear stress - shear rate plot for Newtonian fluid and pseudoplastic (shear thinning) non-Newtonian fluid. Source: Nguyen and Nguyen [22].

The apparent viscosity at very low shear rates is known as the initial viscosity "μ0" and at very high shear rate is known as infinite shear viscosity "μ∞", which is usually defined as the Newtonian viscosity and is very smaller than the shear thinning non-Newtonian viscosity at the aimed shear rate [8]. Thus, the apparent viscosity of the shear thinning non-Newtonian fluids decreases from μ0 to μ∞, when the shear rate increases. For steady flows in pipes and

channels, Equation 1can be generalized by using μ(γ°), a shear-rate-dependent viscosity, and written as:

$$\tau = -\mu(\gamma^\circ) * \gamma^\circ \quad (2)$$

The power-law is simplest and most familiar expression as the generalized Newtonian fluid model, that have been proposed for shear-rate-dependent viscosity μ(γ°)[21].

The power-law model:

$$\mu(\gamma^\circ) = m\gamma^{\circ n-1} \quad (3)$$

Here "*m*" and "*n*" are the characteristic parameters of each fluid that may depend on concentration, temperature, and pressure. The best advantage of using the power-law model is its facility of applications. However, its major disadvantage is the unrealistic apparent viscosity, "μ", of the shear thinning fluid that obtained for the $\gamma^\circ = 0$ and for the $\gamma^\circ \to \infty$; in addition, there is not any time constant parameter in the power-law model while all viscoelastic fluids have characteristics time [21].

Another generalized Newtonian fluid model is Carreau-Yasuda model that corrects the negative features of the power-law model.

***The Carreau-Yasuda model*:**

$$\mu = \mu_\infty + (\mu_0 - \mu_\infty)(1 + (\lambda\gamma^\circ)^2)^{\frac{n-1}{2}} \quad (4)$$

Where "λ" is the time constant and "n" is the power constant. Since the Carreau-Yasuda model has proper compatibility with the shear thinning fluid viscosity behavior, as discussed earlier, it has usually used to demonstrate and predict the dynamic viscosity behavior of the shear thinning non-Newtonian fluids. Additionally, Hyun et al. [8] compared two generalized Newtonian fluid models, power-law and Carreau-Yasuda model, in relation to their adaptability with shear

thinning fluid viscosity behavior; consequently, they presented the result in a log scale graph similar to the graph that is shown in Figure 4.

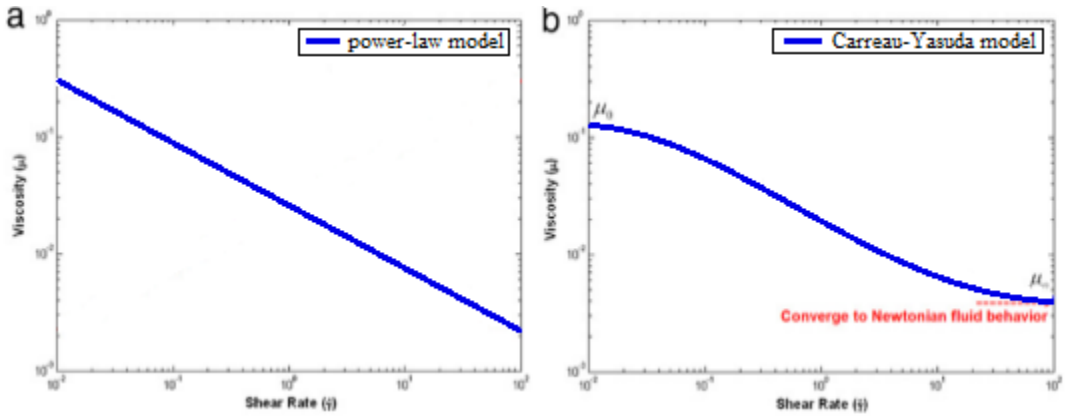

FIGURE 4. Generalized Newtonian fluid model for viscosity in a shear thinning fluid. a) using Power-Law model b) using Carreau-Yasuda model. Source: Hyun et al. [8].

Figure 4, shows the relation between viscosity and shear rate for the shear thinning fluid, blood, using power-law model, graph (a), and using Carreau-Yasuda model, graph (b). It is clear that two graphs behave differently for the very high and the very low values of apparent viscosity. On the other hand, blood was the shear thinning fluid that was investigated there, and the viscosity of blood and its behavior converges to the Newtonian fluid viscosity and behavior at the same very large shear rate [8]; as the result, the Carreau-Yasuda model well described the shear thinning non-Newtonian fluid viscosity behavior.

Finally, the Carreau-Yasuda model is considered the suitable generalized Newtonian model to describe the shear thinning high viscose sealant, and the CFD simulations of this study will carry out using this model.

2.4 Governing Equations and Boundary Conditions

In this study, the flow through the nozzle assumed to be laminar, incompressible, and isothermal. Reynolds number, shown in Equation 5, of the flow inside the nozzles, can be considered the flow regime indicator.

Reynolds number:

$$Re=\rho\frac{vD}{\mu} \quad (5)$$

Here "v" is the velocity of the flow, "ρ" is the density of the sealant, "D" is the hydraulic diameter of the nozzle, and "μ" is the dynamic viscosity of the sealant. In this study, the maximum diameter and cross section area of the nozzles are 1.98E-2 m and 1.23E-3 m, respectively. Dynamic viscosity term in Equation 5 is considered the initial viscosity of the sealant material; as the result, it can be simply verified that the sealant Reynolds number is in the laminar regime domain for the internal flow.

Further, the characteristics dimensions of the nozzles investigated in this study are much longer than sealant material's intermolecular distance, which is the length scale that characterizes the molecular structure of the fluid; therefore, the continuum assumption of the fluid is perfectly valid in this study [9]. Moreover, the continuum assumption will be confirmed later in this study as well, by the CFD simulation results.

According to the above valid assumptions, the Navier-Stokes equation can be employed perfectly for the numerical analysis and design optimization purpose, in this study. The governing equations of the flow include the continuity and the momentum equations are presented in Equation (6) and Equation (7) [23].

***Continuity Equation*:**

$$\nabla v=0 \quad (6)$$

Momentum Equation:

$$\rho\frac{Dv}{Dt}= -\nabla p - [\nabla\tau] + \rho g = -\nabla p + [\nabla\mu * \dot{\gamma}] + \rho g \quad (7)$$

Here "v" is the fluid velocity, "ρ" is the fluid density, "t" is the time, "p" is the fluid pressure, "g" is the gravitational acceleration, "$\dot{\gamma}$" is the shear rate, "μ" is the apparent viscosity of the fluid, and "τ" is the stress tensor as we already defined.

Based on what Zikanov described in his CFD book [24], there are various types of boundary conditions include Dirichlet type, Neumann type, Robin (mixed) type, and Periodicity type. These boundary conditions employ when the flow governing equations in a fluidic system are elliptical. Most of the equations and problems that solved by CFD soft wares are more complicated than they can be categorized simply into these types; thus, only the similarity of the boundary conditions of this study with the aforementioned boundary condition types can be mentioned. Following are the three boundary conditions considered in this study:

The entry: The inlet boundary condition is set up as mass flow inlet, which is similar to the Dirichlet type boundary condition.

$$\dot{m}=2.5\frac{gr}{s} \qquad \textit{Constant mass flow rate on inlet domain} \qquad (8)$$

The exit: The outlet boundary condition is set up as pressure outlet, which is similar to the Neumann type boundary condition.

$$\frac{\partial P}{\partial n}(x,t)=p=101325.0\ Pa \quad \textit{Constant pressure on outlet domain} \qquad (9)$$

The value imposed at the outlet is a constant static pressure of the laboratory and known as the back pressure.

The solid-liquid interface: The wall boundary condition is set up as no-slip boundary condition, which is similar to the Dirichlet type boundary condition.

$$u=0 \qquad \textit{on wall domain} \qquad (10)$$

CHAPTER 3

MODELING, CFD SIMULATIONS AND ANALYSIS

3.1 Modeling

This study focuses on the nozzle geometry optimization for shear thinning high viscous sealant. The critical effective geometrical parameters in nozzles were determined in two ways: First, by investigating through the previous studies on nozzle geometry optimizations as discussed in previous chapter; the other way, by considering the commercially available Semco sealant applicant nozzles. Figure 5 illustrates the defined geometry parameters.

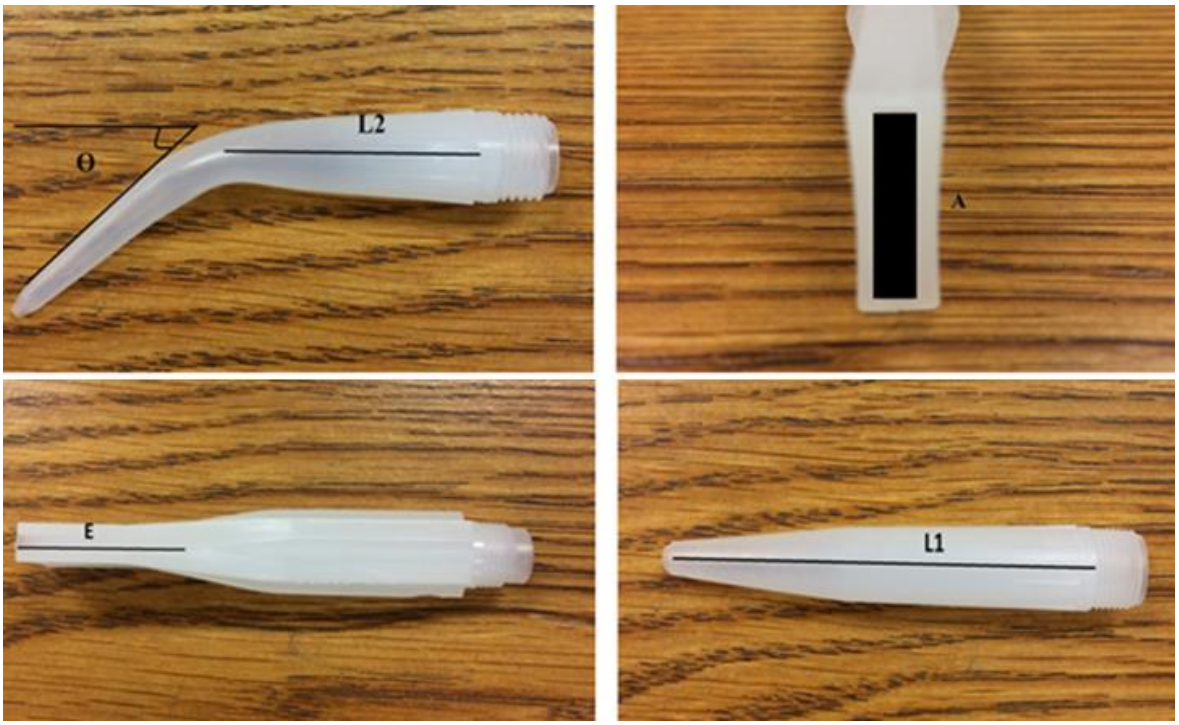

FIGURE 5. Nozzle geometry parameters.

Where "L1" is entire length of the nozzle, "A" is outlet cross section area, "E" is existence of the extension part, "L2" is length of the straight part of the nozzle, and "Ɵ" is the bent angle.

The various 3D nozzle models were defined by using these parameters. Table 1 shows the complete list of these models and parameters.

TABLE 1. Effective Geometry Parameters

Model	L1 (in.)	A (in. sq.)	O	E	Θ (degree)	X	L2 (in.)
1	2.5	0.1227	1	0	0	1	0
2	2.5	0.04908	1	0	0	1	0
3	4	0.01227	1	0	0	1	0
4	4	0.00306	1	0	0	1	0
5	8	0.04908	1	0	0	1	0
6	4.375	0.04908	1	0	0	1	0
7	3.4375	0.09375	0	1	0	0	0
8	4.5	0.09375	0	1	0	0	0
9	4	0.09375	0	1	0	0	0
10	4	0.00306	1	0	30	0	1
11	4	0.01227	1	0	20	0	2
12	4	0.01227	1	0	30	0	2
13	4	0.01227	1	0	45	0	2
14	4	0.01227	1	0	30	0	1
15	4	0.01227	1	0	45	0	1.5

Where "Ɵ" is the round shaped outlet section area and "X" is axisymmetric configuration of the nozzle. Afterwards, the CAD software SolidWorks was used to build the nozzle geometry 3D models.

To keep a constant condition for all of the experimental study observations and to decrease the experimental error, each geometry model was considered and built as the module includes the nozzle attached to the sealant cartridge. Detailed explanations for experimental study will be provided in chapter 5.

3.2 CFD Simulations

In order to investigate the sealant flow characteristics, Computational Fluid Dynamics (CFD) simulations were performed with CFD software Star-CCM+ 10.04.011 (Siemens). Following sections present complete software set up package.

3.2.1 3D Geometry Model

The developed 3D-CAD model was imported to the CFD software as parasolid type file. Figure 6 shows the geometry node configuration. The imported 3D model was appeared under Geometry node as Body1. In addition, Body 1 was splitted up by patches into three different surfaces: Inlet, Outlet, and Wall.

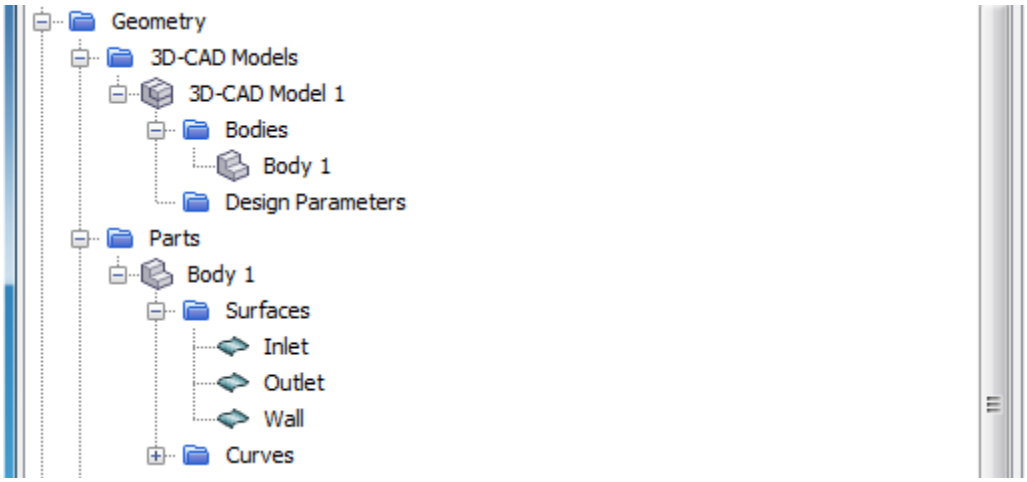

FIGURE 6. Star-CCM+ simulation window.

The geometry parts are used in order to the spatial display of the model. In order to apply the physics to the computational model, the regions and boundaries were created for each part and for each part surface, respectively. Figure 7 exhibits the regions node configuration and Figure 8 exhibits the boundaries in graphic window.

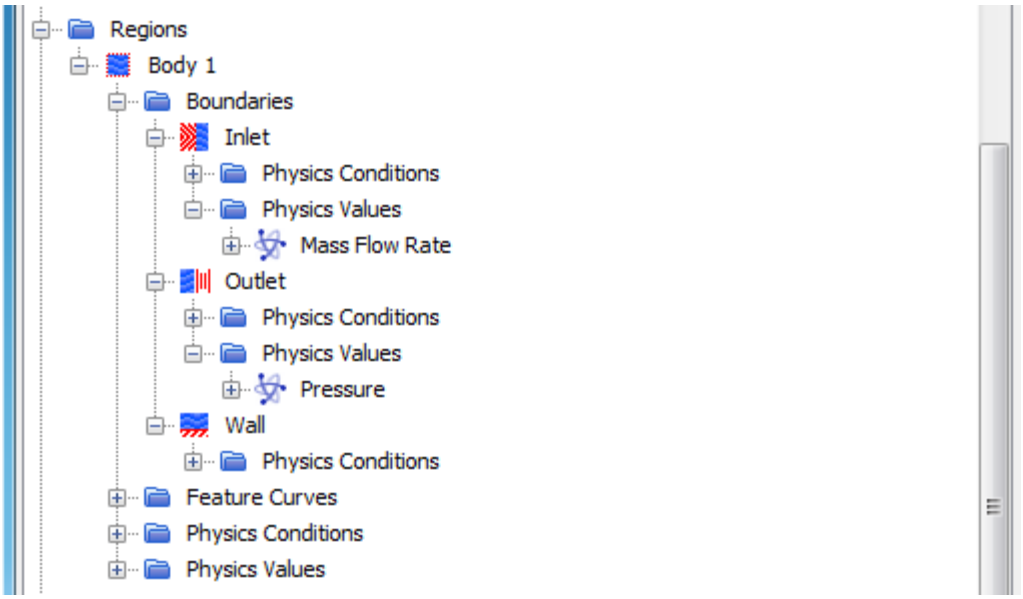

FIGURE 7. Star-CCM+ simulation window.

FIGURE 8. Example of boundaries. (Model #13).

The types of the boundaries were set up in this step based on the boundary condition types that was explained in previous chapter.

3.2.2 Mesh Generation

The mesh or grid is the geometric primitive representation that is used to split the flow domain into smaller subdomains, which let the CFD software discretize and solve the flow governing equations inside them. In this study, Automated Mesh operation was created and applied to the geometry part. Figures 9, 10, and 11 respectively show the "Meshers", "Default Controls", and "Custom Controls" settings that were defined in this study.

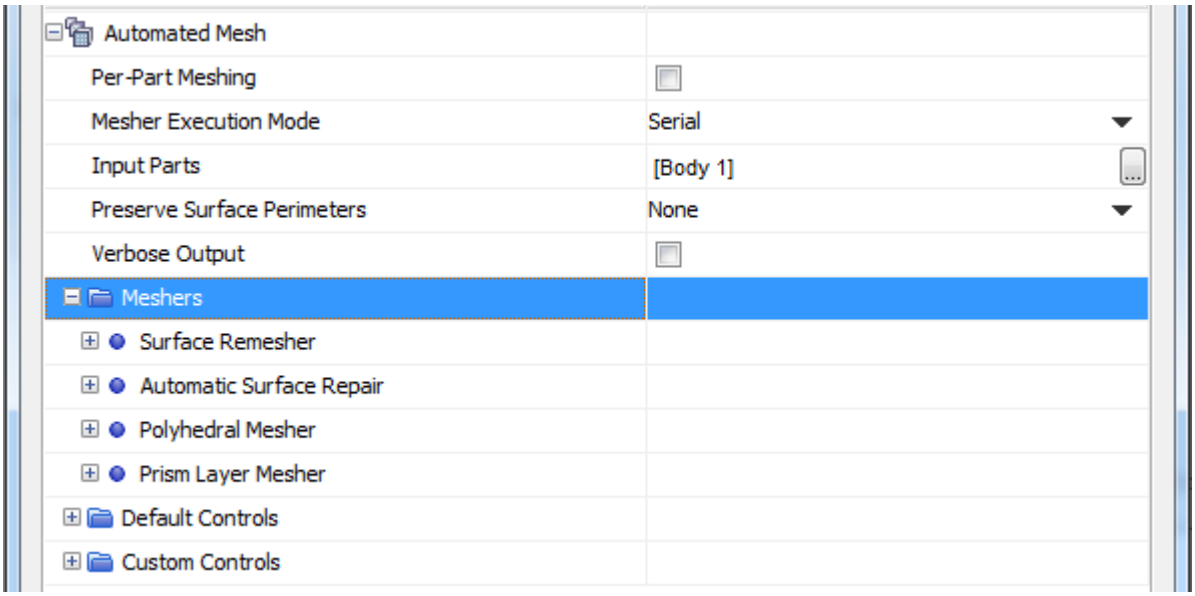

FIGURE 9. Meshers setting.

As it is shown in Figure 9, the "Meshers" was created with "Surface Remesher" tool, which is used to improve the overall quality of the existing surface, and Automatic Surface Repair tool in order to correct the possible geometric type problems; in addition, the "Meshers" was created with polyhedral-shaped volume mesh cells and five layers of prismatic cells that were inserted along the walls.

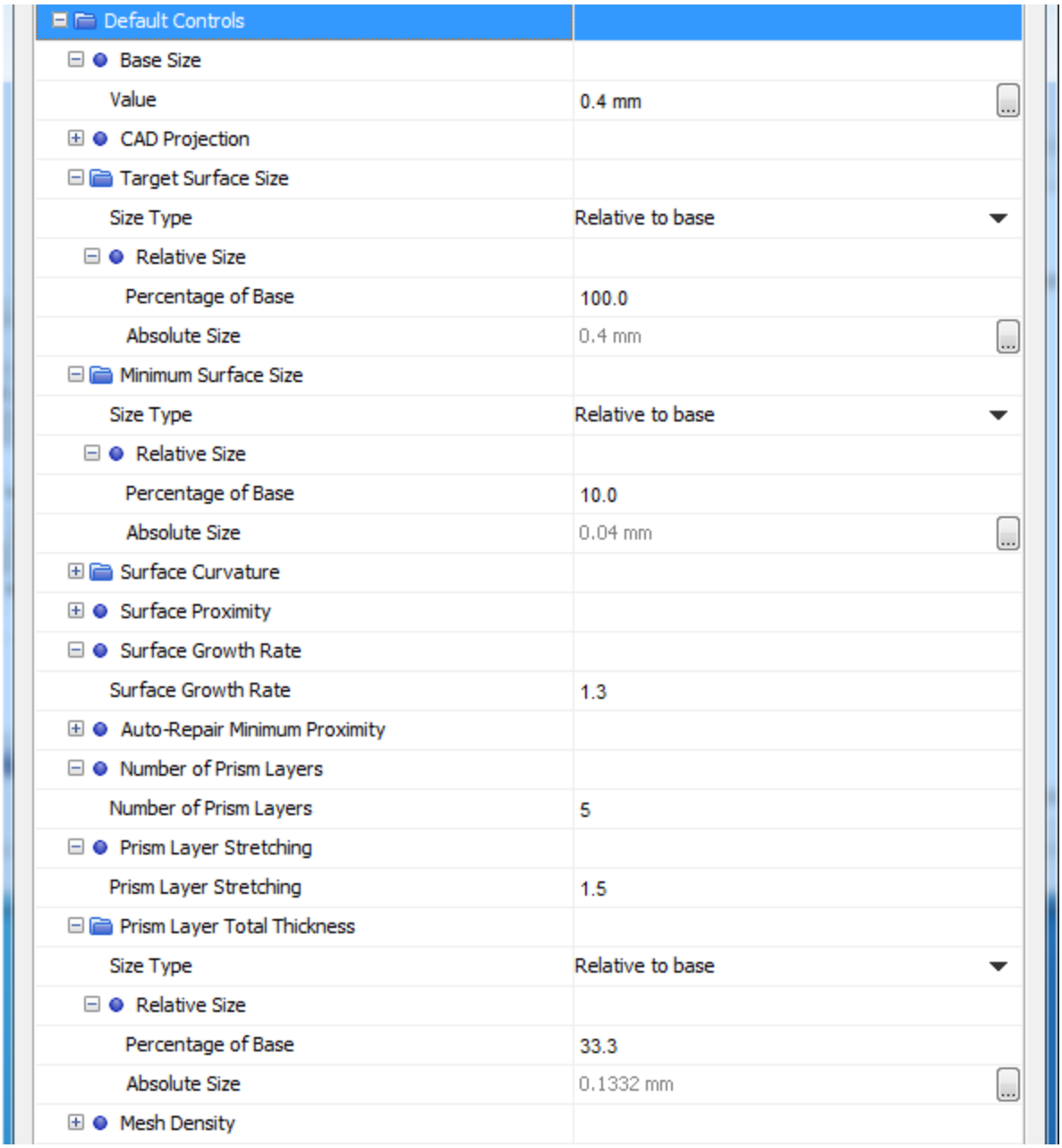

FIGURE 10. Default Controls setting.

As Figure 10 illustrates, "Mesher" properties were managed in "Default Controls" to improve the accuracy of simulation results. For example, the value of the "Base Size", which is a reference length value for all the relative size controls, could be modified here to be compatible with overall geometry dimensions. Here this value is 0.4 mm.

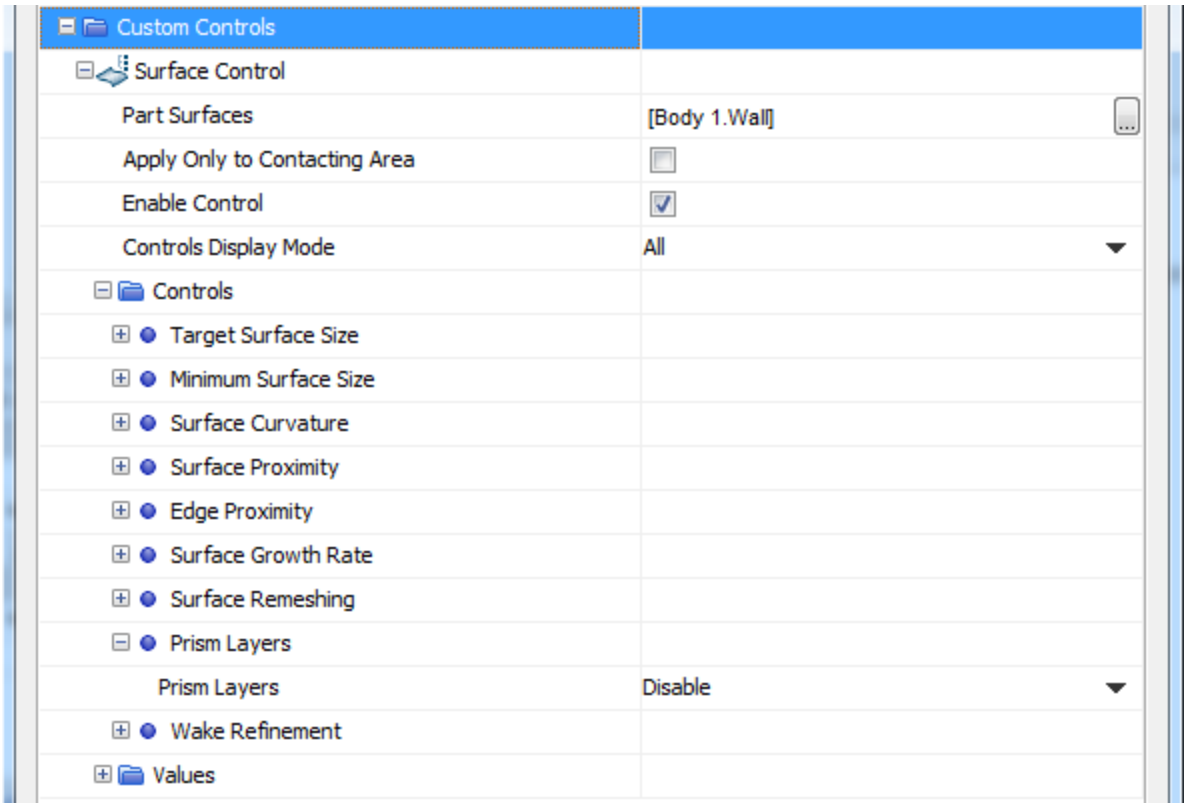

FIGURE 11. Custom Controls setting.

"Custom Controls" operation is a facility to modify the "Meshers" settings to fit in the condition. In this study, as it is shown in Figure 11 a "Surface Control" tool was created in order to modify the "Prism Layers" value. The "Prism Layers" are generated along all the surfaces by default, while they are only required to be generated along the no-slip walls.

3.2.2.1 Mesh independency. It is apparent to validate the mesh independency in the aforementioned CFD simulations. In this study, the mesh-independency of the CFD simulation results was examined for different mesh configurations. First, the domain was meshed with a coarse mesh size, then the solution-adaptive refinement was conducted by comparing the pressure drop, whereas the mesh size improved (became finer) [25]. In each of the iterations in mesh independency convergence graph, the size of target surface cells decreased by 1:2 ratios and the pressure drop was measured for each of the iterations.

In this section, a detailed mesh independency study is shown for the specific nozzle setting model #2. The five separate studies were considered with different mesh sizes made of 1291232, 1364070, 1454871, 2085722 and 5948176 volume cells. Table 2 presents different settings for each of the separate configurations. Figure 12 shows the solution adaptive convergence graph (mesh independency graph) and differences in pressure drop for each one.

TABLE 2. Configurations Comparison

Test #	Target surface cell size (percentages of Base Size)	Volume mesh cells	Pressure drop (pa)	Pressure drop Differences $dp_n - dp_{n-1}$
1	1600 %	1291232	6.653744E+04	------
2	800%	1364070	6.658601E+04	0.0002883%
3	400%	1454871	6.656959E+04	-0.0012842%
4	200%	2085722	6.648410E+04	-0.0002465%
5	100%	5948176	6.650327E+04	0.00072995

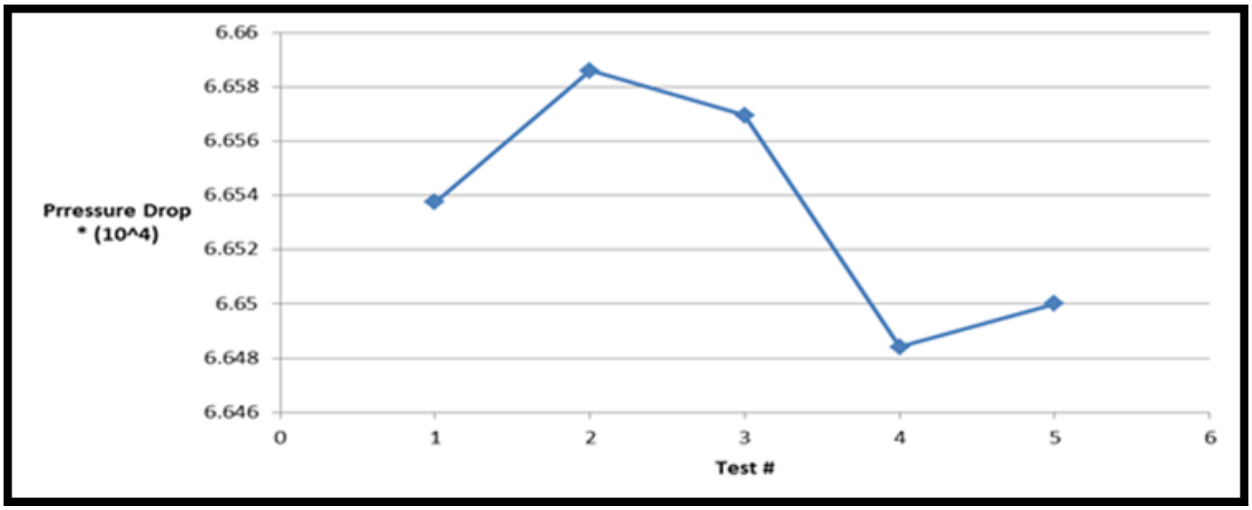

FIGURE 12. Solution-adaptive graph.

As the above graph and table clearly indicate, pressure drop differences in all cases were less than 0.001%. Almost all iterations confirmed that the results were independent from the mesh size. Although all of the five mesh configurations technically led to the mesh independent solution, the finest one (#5) was picked to conduct the simulation. The same mesh independency solution check procedure was carried out for each model, the details are not provided here to avoid redundancy of information, and CFD simulation was ran with the finest mesh in each model.

3.2.3 Physics Continua Definition

A physics model defines the mathematical governing equations and the primary variable parameters of the simulation such as pressure and velocity. Figure 13 shows the physics models that were selected in this study.

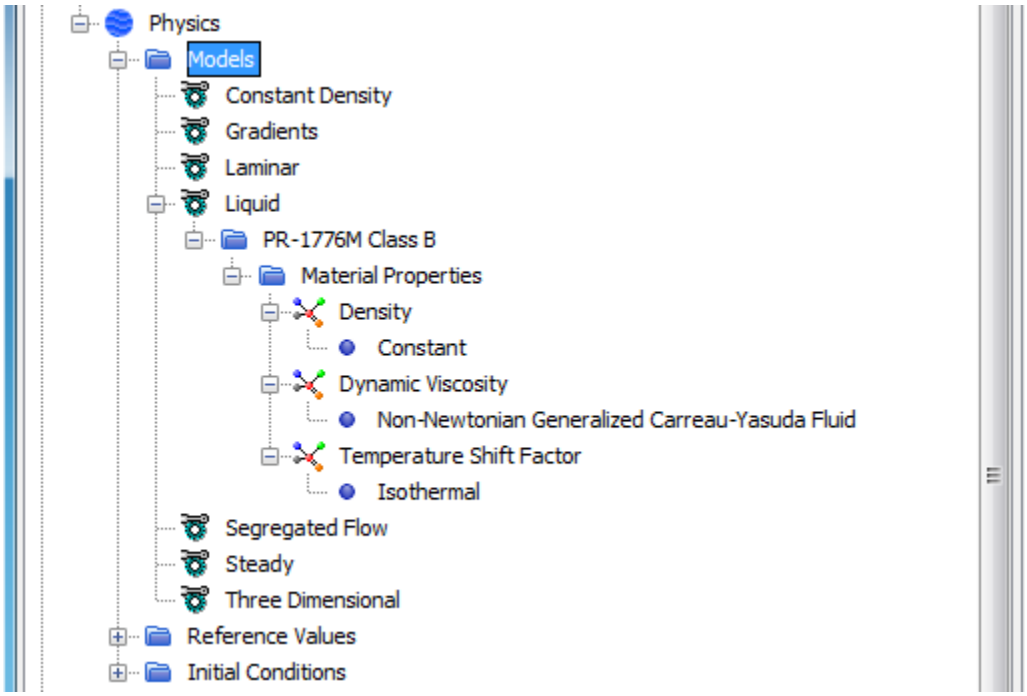

FIGURE 13. Physics model of the flow.

In this study, Segregated Flow model with the 2nd-order convection upwind scheme was selected to be compatible with the incompressible sealant material and its low inlet flow velocity.

Density of the fuel tank sealant PR-1776M Class B is 1250Kgm^3, which was provided by PPG Aerospace Research and Technology. The flow reasonably was considered Isothermal since this study was not carried out for harsh temperature change conditions.

As it was discussed in Introduction and Literature Review chapters, the generalized Newtonian Carreau-Yasuda model, Equation (4), was the best compatible option to describe the dynamic viscosity behavior and distribution of the shear thinning high viscous sealant material.

The Carreau-Yasuda model:

$$\mu=\mu_\infty + (\mu_0-\mu_\infty)(1 + (\lambda\gamma^\circ)^2)^{\frac{n-1}{2}} \quad (4)$$

Figure 14 illustrates five parameters of this model and the values that were set on them in this study.

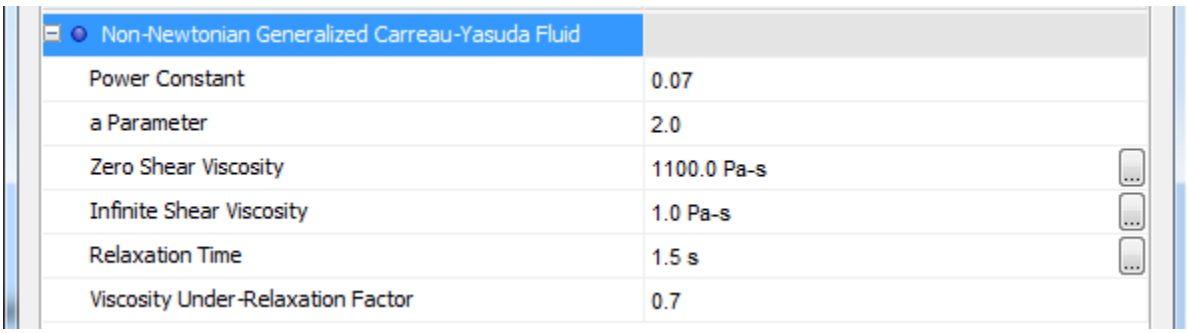

FIGURE 14. Carreau-Yasuda model properties.

In this study, the Relaxation Time constant "λ", Viscosity Under-Relaxation Factor, which is an expert property of the model in Star-CCM+, and the *"a"* parameter, which is a parameter to control the shear-thinning property [26], were left with their default values. Further, 0.07 was set on the power constant *"n"* by investigating through the tabulated typical values of power constant for a few systems [22].

The Zero Shear Viscosity *"*μ_0*"* value was provided by PPG Aerospace Research and Technology. In addition, by considering the water as the least possible viscous incompressible

fluid, the Infinite Shear Viscosity "μ_∞" value was reasonably assumed the same as water dynamic viscosity value, 1 Pa.S.

Although in steady state model, the solution converges independent of the initial field values, the initial conditions affect convergence pattern and computing power cost. Here, the initial conditions were set as 101325 Pa and 0 on pressure and velocity, respectively.

3.3 CFD Analysis

3.3.1 Theory

In this study, the nozzle geometry optimization was done in order to approach the minimum pressure drop and minimum overall dynamic viscosity of the sealant throughout the nozzle.

By appearing the shear rate throughout the nozzle flow, dynamic viscosity of the shear thinning sealant decreases. Therefore, the flow ability of the sealant increases, which leads to avoid stagnation point creation. In addition, by decreasing the sealant pressure drop throughout the nozzle, the less energy is required to make the sealant flow inside the nozzle.

Investigation into the flow governor Equation (6) and Equation (7) confirms that pressure drop and dynamic viscosity change in the same way. Figure 15, demonstrates an infinitesimal general volume control element.

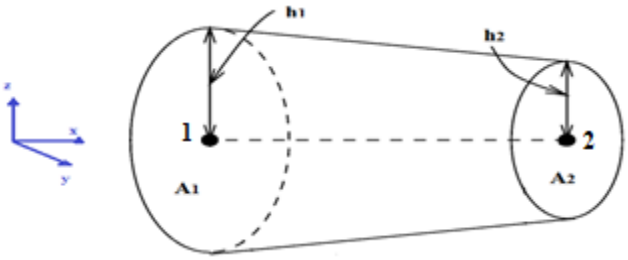

FIGURE 15. Infinitesimal volume control.

By moving from point 1 toward point 2 in x direction, cross section area and distance to the wall decreases, $A_2 < A_1$ and $h_2 < h_1$; thus, to keep the constant mass flow rate, shear rate "$\dot{\gamma}$"

and velocity "*v*" increase from point 1 to point 2. As it was demonstrated in Figure 3 and Figure 4, when shear rate increases, shear stress "τ" increases but apparent viscosity "μ" decreases.

Moreover, the left hand side of momentum equation, Equation (7), ($\rho\frac{Dv}{Dt}$) is zero due to steady state flow condition. Since the momentum equation is applied for x direction in this study, the gravity term does not appear and the 3rd term in right hand side (ρ g) is zero. Equation (11) is approached as the result.

Momentum Equation:

$$\rho\frac{Dv}{Dt} = -\nabla p - [\nabla \tau] + \rho g \qquad (7)$$

X-direction Momentum Equation:

$$0 = -\nabla p - [\nabla \tau] \rightarrow -\nabla p = [\nabla \tau] \qquad (11)$$

In Equation (11), since "∇p" shows pressure or pressure drop changes, "-∇p" has positive value in the left hand side; consequently, "[∇τ]" that shows changes in shear stress has positive value and shows increase in shear stress.

It is confirmed that, when the shear rate increases in shear thinning sealant, the dynamic viscosity decreases. Further, sealant pressure drop and sealant dynamic viscosity change in the same way.

3.3.2 CFD Scenes and Reports

In STAR-CCM+ software, a scene is used to monitor the solution and visualize the simulation. In this study, scenes were created to observe the dynamic viscosity behavior, velocity vectors, velocity streamlines of the flow, and pressure distribution of the simulation.

Different plane sections were created along the nozzle centerline. A streamlines section was created as well. Figures 16 to 19 present examples for the scenes of this study, although all

of the scenes will be presented in Appendix C.

Figure 16 shows the dynamic viscosity distribution scene in two different plane sections of model #7. The scalar bar, maps values to colors by the value indicators alongside a color spectrum bar.

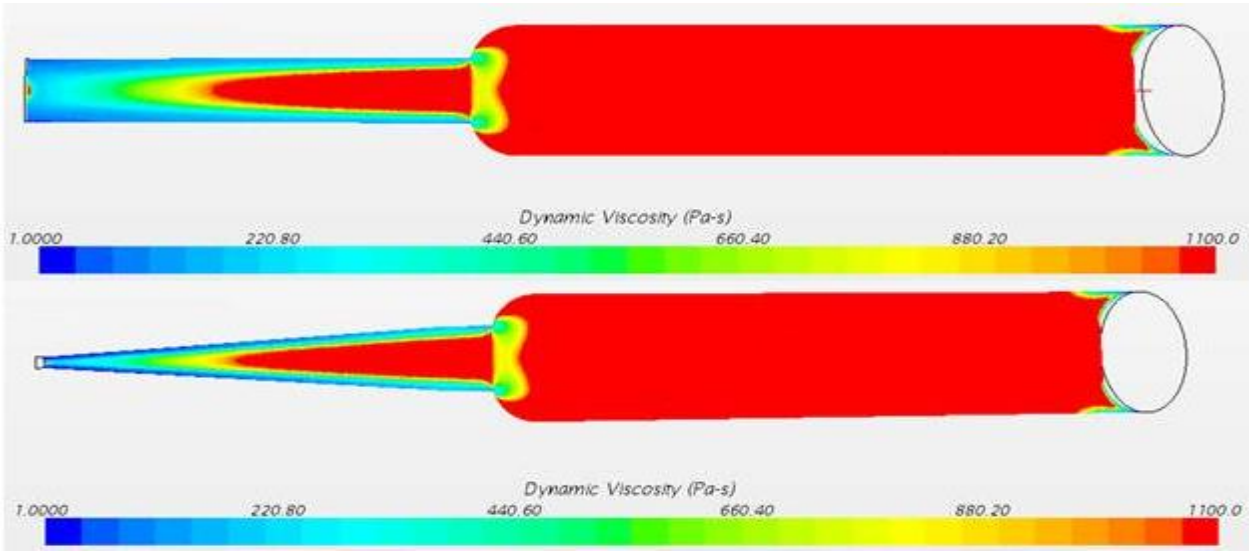

FIGURE 16. Dynamic viscosity distribution. (Model #7).

In Model #7, when flow moved from larger cross section area toward smaller one, sealant dynamic viscosity decreased outstandingly and reached to its minimum value at the smallest cross section area very close to the nozzle outlet. The result is compatible with what is expected theoretically. Further, it can be considered that nozzle extension part effects on the overall value of sealant dynamic viscosity.

Figure 17 shows the static pressure distribution for Model #12.

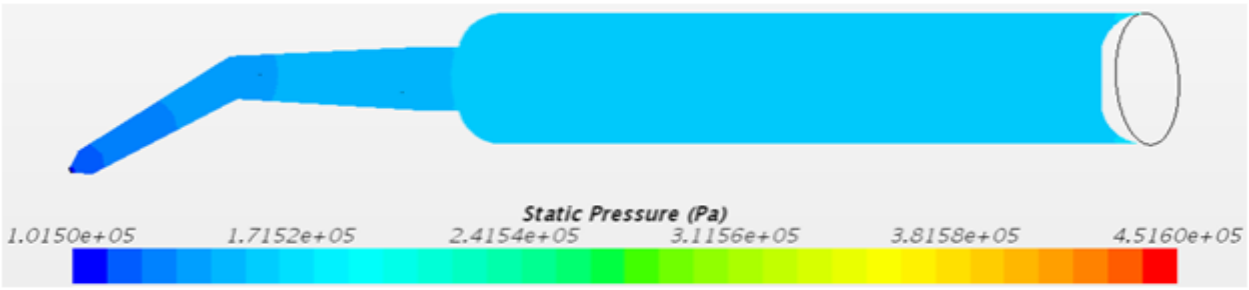

FIGURE 17. Static pressure. (Model #12).

As it is shown in Figure 17, pressure decreased from the module inlet toward its outlet. Major changes occurred after the bent section in the end part of the nozzle; thus, the flow pressure was impressed by the bent section inside the nozzle.

Figure 18 shows the velocity vectors for Model #10.

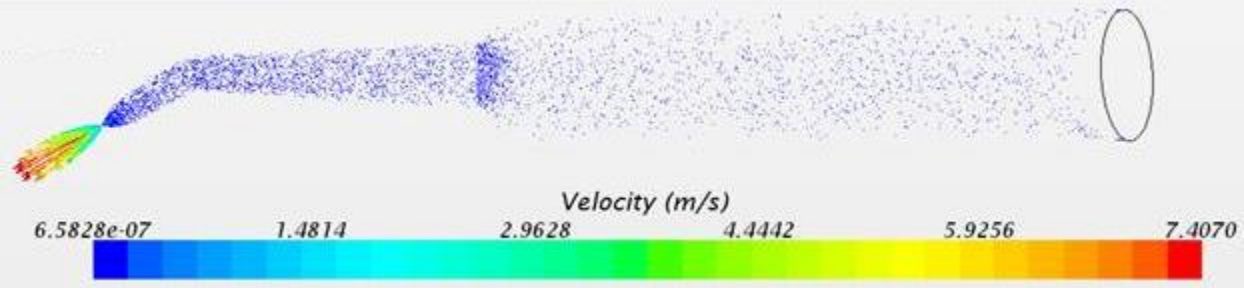

FIGURE 18. Velocity vectors. (Model #10).

As it is demonstrated in Figure 16, the velocity vectors along the module, reached to their highest magnitude at the nozzle outlet cross section. Similar to the pressure changes that was shown in Figure 17 the changes in velocity were more noticeable after the bent section.

In this study, it can be reasonably concluded that pressure distribution, velocity changes, and dynamic viscosity behavior of the flow inside the nozzle in different nozzle geometry models are almost compatible.

Figure 19 is a streamlines scene for Model # 10.

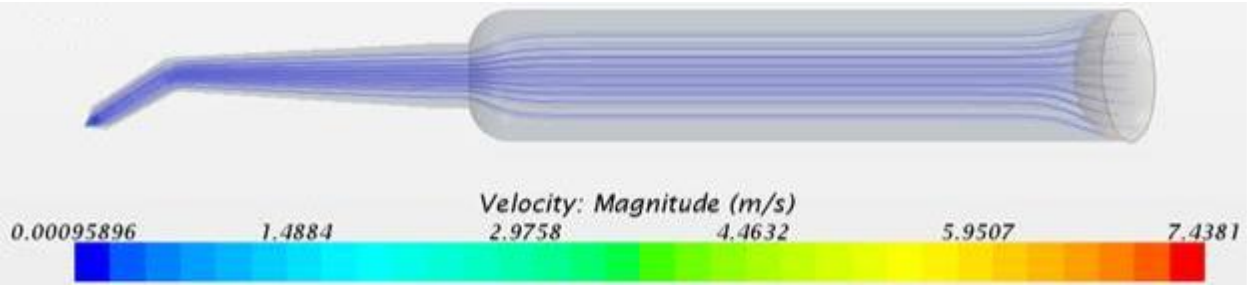

FIGURE 19. Velocity streamlines. (Model #10).

The laminar flow regime is demonstrated by the straight streamlines along the module length. Moreover, the lack of stagnation points and material clogging points inside the nozzle

flow was confirmed by the straight streamlines that are shown in Figure 19.

The accurate sealant pressure drop values, from inlet to the nozzle outlet, were required to be used for optimization purpose. The values were obtained from CFD software as the numerical solution results. They are presented in next section.

3.3.4 Simulation Results

Table 3 presents the complete list of pressure drop values from inlet to the nozzle outlet. The overall values of dynamic viscosity in each module are presented in Table 3, as well. The values were reported by CFD software and were related to the point, at which the stopping criteria was satisfied and the iterations were stopped. In this study, the stopping criteria were set to continuity residual amount of 1E-07.

TABLE 3. Simulation Results Table

Model #	Pressure Drop (pa)	Volume Average Dynamic Viscosity (Pa.s)	Model #	Pressure Drop (pa)	Volume Average Dynamic Viscosity (Pa.s)
1	6.6504E+04	9.913706E+02	9	2.69132E+06	9.651243E+02
2	6.95004E+04	9.913679E+02	10	1.24226E+05	9.812123E+02
3	1.26292E+07	9.798357E+02	11	7.28004E+04	1.033114E+03
4	1.35423E+05	9.799611E+02	12	1.25847E+07	9.807678E+02
5	6.609586E+04	9.798531E+02	13	1.256502E+07	9.802881E+02
6	9.63139E+04	9.519211E+02	14	7.80473E+04	9.801619E+02
7	6.19036E+04	1.028243E+03	15	7.93414E+04	9.803380E+02
8	5.39059E+04	1.035712E+03			

CHAPTER 4

METHODOLOGY

4.1 Design of Experiments (DOE)

The main goal of this study is geometry optimization and the Response Surface Methodology (RSM) is used for data collection, mathematical modeling, and optimizing the effective parameters. Technically, RSM is the process and product optimization method by using Design of Experiments. The application of RSM is common in a situation with some input variables that possibly influence the quality characteristics or performance of the process or the product.

Likewise, in this study there are some nozzle geometry features that influence the pressure drop and dynamic viscosity behavior of the sealant material throughout the nozzle, and influence amount of air bubbles trapped within the sealant inside the nozzle. Here, these geometry features were considered the input variables and the pressure drop from nozzle inlet to the outlet was considered the system performance or the response. Thereafter, a 2nd order regression model was developed to mathematically represent the effect of the parameters on the response.

This model is basically an empirical model based on the observation data from the process of sealant flow inside the nozzle.

4.1.1 Design of Experiments (DOE) Layout

As they were listed in Table1, there were seven parameters or geometry features that were considered the input variables. Pressure drop values that were listed in Table 3, considered the response parameter. The linear regression model with seven continuous predictors

(input variables) was implemented in Minitab® 18.1 software. The DoE layout is shown in figure 20.

Worksheet 1 ***

↓	C1	C2	C3	C4	C5	C6	C7	C8
	L1	A	O	E	Θ	X	L2	P
1	2.5000	0.01227	1	0	0	1	0.0	66504
2	2.5000	0.04908	1	0	0	1	0.0	69500
3	4.0000	0.01227	1	0	0	1	0.0	12629200
4	4.0000	0.00306	1	0	0	1	0.0	135423
5	4.0000	0.04908	1	0	0	1	0.0	66096
6	8.0000	0.04908	1	0	0	1	0.0	96314
7	4.3750	0.09375	0	1	0	0	0.0	61904
8	3.4375	0.09375	0	1	0	0	0.0	53905
9	4.5000	0.09375	0	1	0	0	0.0	2691320
10	4.0000	0.00306	1	0	30	0	1.0	124226
11	4.0000	0.01227	1	0	20	0	2.0	72800
12	4.0000	0.01227	1	0	30	0	2.0	12584700
13	4.0000	0.01227	1	0	45	0	2.0	12565020
14	4.0000	0.01227	1	0	30	0	1.0	78047
15	4.0000	0.01227	1	0	45	0	1.5	79341

FIGURE 20. DoE layout.

In order to obtain the regression model, stepwise elimination method was used. For this method, the Alpha-to-remove/Alpha-to-enter were reasonably considered 0.3. This 0.3 significance level was based on several factors such as the model robustness and prior successful data collections for this experiment.

Figure 21 shows the complete Analysis of Variance (ANOVA) table and Figure 22 shows the final regression model that was obtained.

Regression Analysis: P versus L1, A , O , E , Θ , X , L2

Stepwise Selection of Terms

α to enter = 0.3, α to remove = 0.3
The stepwise procedure added terms during the procedure in order to maintain a hierarchical model at each step.
Beginning with step 2, the model may not be hierarchical because some required terms are impossible to estimate.

Analysis of Variance

Source	DF	Adj SS	Adj MS	F-Value	P-Value
Regression	3	2.27083E+14	7.56944E+13	5.87	0.012
Θ*Θ	1	1.39475E+14	1.39475E+14	10.81	0.007
L2*L2	1	1.06199E+14	1.06199E+14	8.23	0.015
Θ*L2	1	1.41939E+14	1.41939E+14	11.01	0.007
Error	11	1.41870E+14	1.28973E+13		
Total	14	3.68953E+14			

FIGURE 21. ANOVA table.

Regression Equation

P = 1722849 - 39694 Θ*Θ - 11800384 L2*L2 + 1546771 Θ*L2

FIGURE 22. Regression model.

By investigating the ANOVA table and the identified regression equation, parameters L2 and Θ were found as the most significant factors in this optimization process. As it is shown in Figure 22, the regression equation comprises the second-order terms of L2, the second-order terms of Θ, and the linear interaction term of them; however, does not comprise their first-order terms.

By adding more variables to a regression model, its sum of squares for regression increases and its error sum of squares decreases; although it does not necessarily mean that all of those variables are statistically significant [27]. Thus, to reach the more accurate regression

model, a linear regression model with two parameters L2 and Θ, continuous predictors, was implemented.

Figure 23 presents the ANOVA table and Figure 24 presents the regression model respectively.

Regression Analysis: P versus L2, Θ

The following terms cannot be estimated and were removed:
L2*Θ

Analysis of Variance

Source	DF	Adj SS	Adj MS	F-Value	P-Value
Regression	4	2.27240E+14	5.68100E+13	4.01	0.034
Θ	1	8.51863E+13	8.51863E+13	6.01	0.034
L2	1	1.13255E+14	1.13255E+14	7.99	0.018
Θ*Θ	1	7.04891E+13	7.04891E+13	4.97	0.050
L2*L2	1	1.29867E+14	1.29867E+14	9.16	0.013
Error	10	1.41713E+14	1.41713E+13		
Lack-of-Fit	1	2.90885E+12	2.90885E+12	0.19	0.674
Pure Error	9	1.38804E+14	1.54227E+13		
Total	14	3.68953E+14			

FIGURE 23. ANOVA table.

Regression Equation

P = 1753185 + 3015035 Θ - 91375866 L2 - 38461 Θ*Θ + 34162304 L2*L2

FIGURE 24. Regression model.

As it is shown in Figure 24, the regression equation compromised the first-order term of L2, the first-order term of Θ, and their second-order terms. Here, the identified regression model is the multiple linear regression response surface model with two independent variables L2 and Θ. The complete list of DoE tables will be presented in Appendix D.

4.1.2 DOE Data Analysis

The significance effects of each factor and interactions of the factors on the optimization process can be studied by analyzing DoE tables and plots. Figure 25 shows the normal

probability plot. This plot is used to check the normality assumption. In this study, the normality assumption was confirmed since most of the residual points were almost along a straight line.

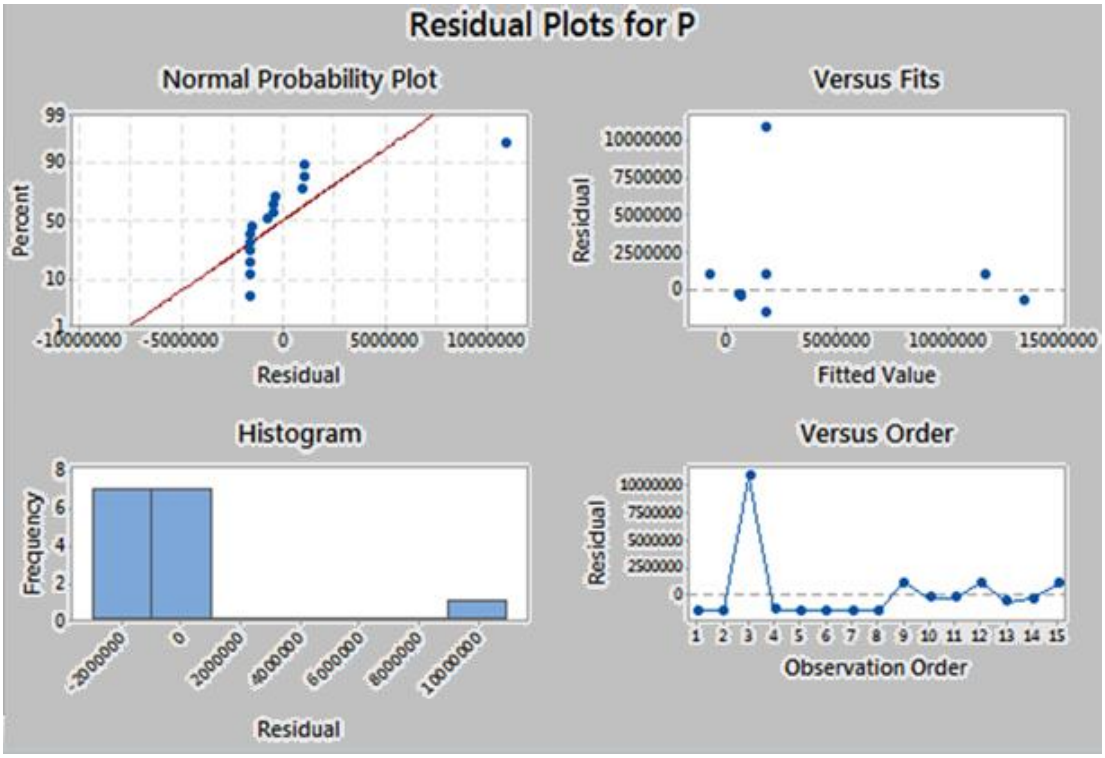

FIGURE 25. Residual plot for response P.

The sensitivity analysis was implemented for two factors L2 and Θ. Figure 26 illustrates the main effects plot.

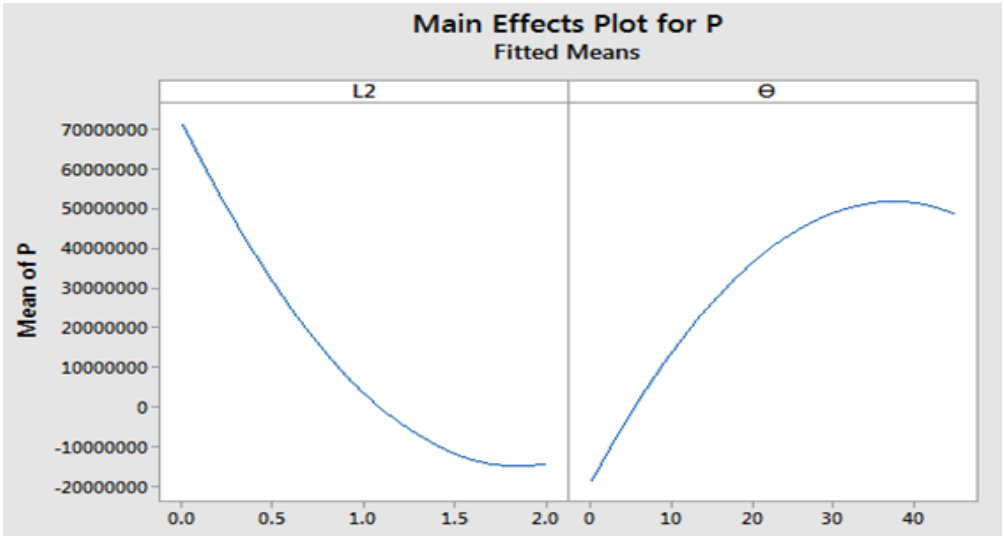

FIGURE 26. Main effects plot for response P.

The mean value of pressure drop was plotted for each of the two factors L2 and Θ to examine how the factors influence the response. As it can be observed in Figure 26, the response is more sensitive to the smaller values of factor L than its larger values; likewise, the response is more sensitive to the smaller values of factor Θ than its larger values.

Contour plot of the response P versus two significant factors L2 and Θ, is shown in Figure 27.

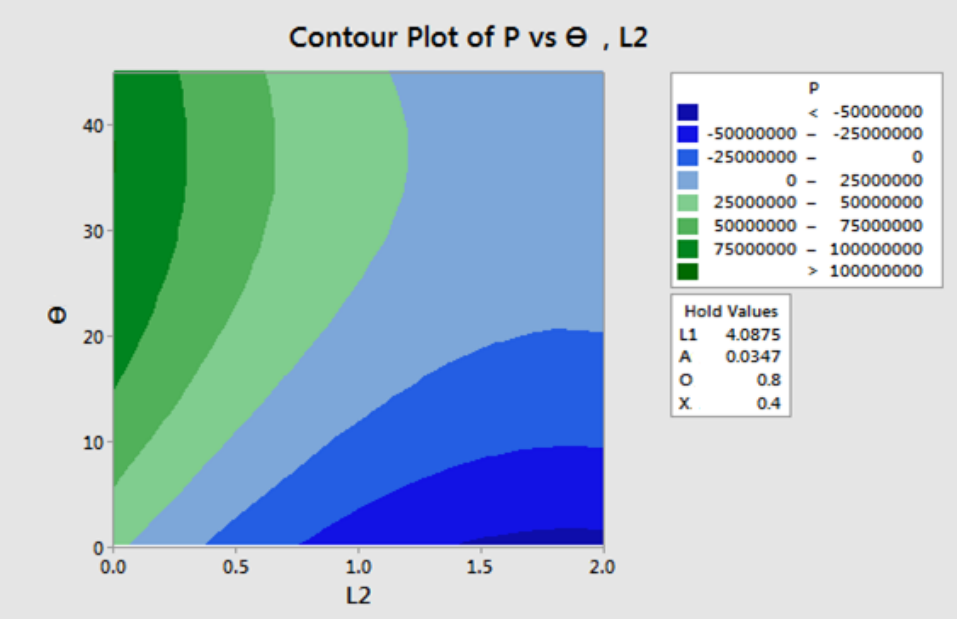

FIGURE 27. Contour plot of response P versus Θ and L2.

In Figure 27, it can be observed that the pressure drop increases dramatically by increasing the Θ, from 0 to 45 degree, when the L2 has its lowest value 0; however, pressure drop decreases slightly by increasing the L2 from 0 to 2, when the Θ is in its lower setting 0.

Figure 28 illustrates the surface plot of response P versus two factors L2 and Θ. This 3D response surface was plotted based on the observations data. As it can be observed in Figure 28, the pressure drop increases intensively when two factors L2 and Θ increase simultaneously.

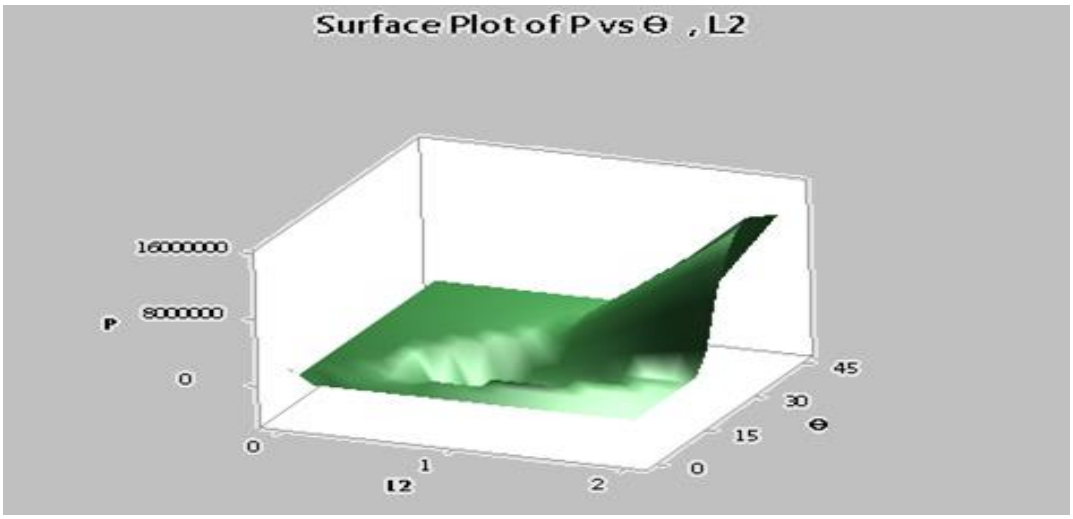

FIGURE 28. Surface plot of response P versus L2 and Θ.

In addition, the response surface plot and its contour lines in this study were created by Mat Lab software. Figure 29 shows the surface, which was fitted to the 15 data points related to the 15 observations, and its contour lines.

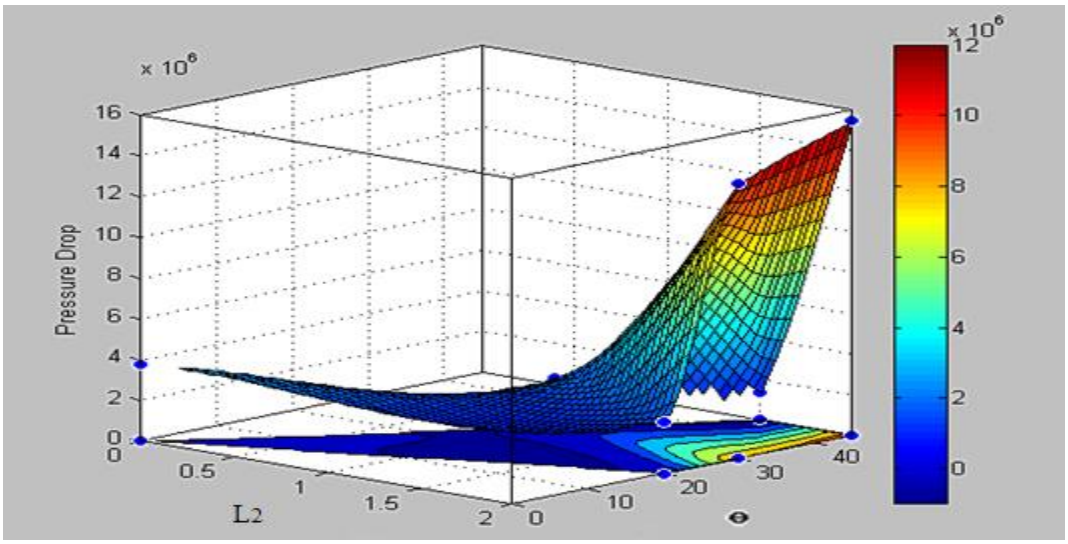

FIGURE 29. Surface fitted to the observations data.

This surface can be considered rising ridge surface type, which is a kind of surface defined for the model that includes second-order terms with two variables [27].

Figure 30 shows the surface, which was fitted to the identified regression model, and its contour lines.

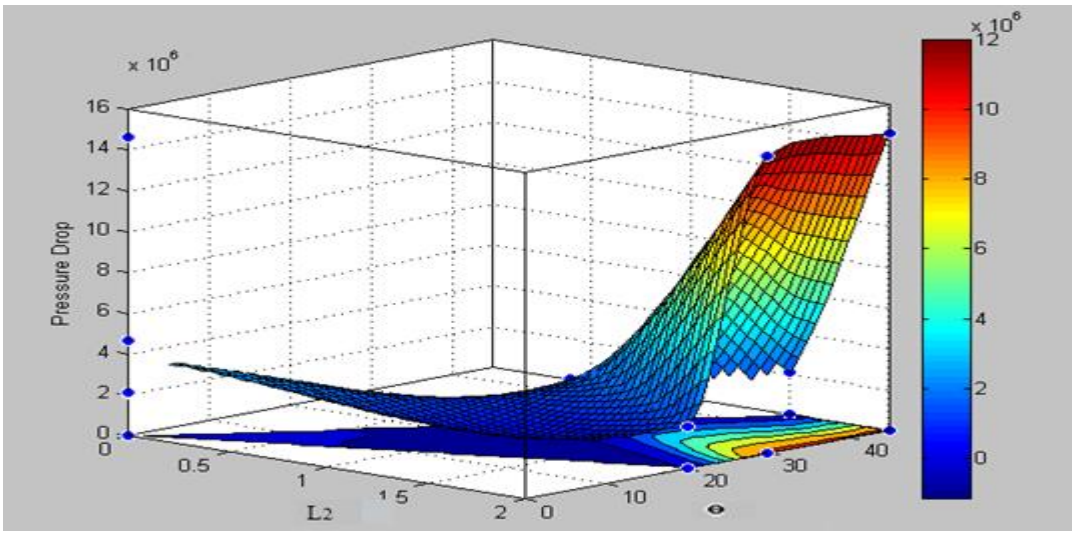

FIGURE 30. Surface fitted to the regression model.

Figure 31 shows the aforementioned surface and their difference surface, in the same figure.

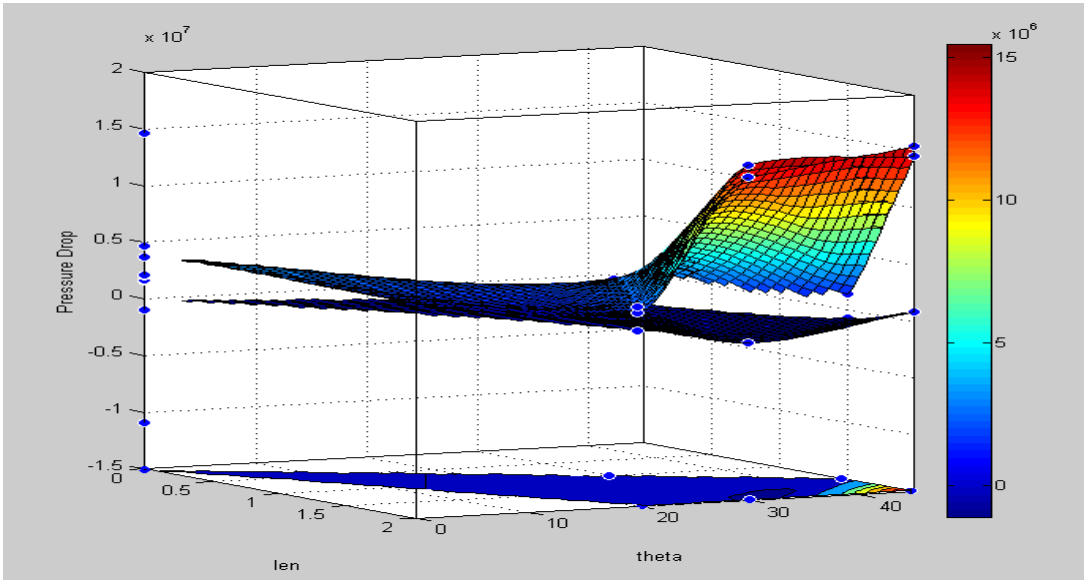

FIGURE 31. Surface comparison.

4.1.3 Response Optimization

DOE was conducted in this study to identify the response surface model that lead to minimum sealant pressure drop throughout the nozzle. To find the assigned values to the variables in this model, the response optimizer tool in Minitab was used. The target was

considered zero response to get the best fitted response value and compatible values for variables L2 and Θ. Figure 32 shows the response optimizer predicted values.

Response Optimization: P

Prediction for P

Multiple Response Prediction

Variable	Setting
L2	0.0191657
Θ	0

Response	Fit	SE Fit	95% CI	95% PI
P	14455	1377737	(-3055334, 3084244)	(-8917428, 8946338)

FIGURE 32. Response optimization: P.

The predicted values are 0.0191657 for L2 and 0 for Θ, when response was fitted to 1.44553E+04. The confidence Interval of the prediction was 95%.

In this study, there were five more variables that were recognized as the less significant variables in early steps of DoE procedure; however, those were the real physical geometrical features with magnitude. Thus, the response optimizer tool was used one more time. The values 0, 0, 0.0191657 were considered for response, Θ, and L2 respectively, in first identified regression model. Figure 33 shows the response optimizer predicted values with 95% confidence Interval.

Response Optimization: P

Multiple Response Prediction

Variable	Setting
L2	0.0191657
Θ	0
L1	5.94444
A	0.09375
O	0.005088
X	0.0141114

Response	Fit	SE Fit	95% CI	95% PI
P	15954	4329478	(-54995276, 55027183)	(-59232968, 59264876)

FIGURE 33. Response optimization: P.

The predicted values were 5.94444, 0.09375, 0.005088, and 0.0141114 for L1, A, O, and X variables, respectively. Some of the input variables were real physical parameters and were able to get only two possible values 0 and 1; as the result, these values were explicated to be compatible with their real physical conditions. Thus, the values of both O and X were changed to 0; in addition, since A referred to the specific models #6, #7, and #8, value of E was considered 0.

By investigation into the 3D surface plot, Figure 28, it was figured out that by increasing two variables Θ and L2, the response increase; on the other hand, the goal was minimizing the pressure drop. Consequently, another response optimizing process carried out for Θ=0 and L2=0 to obtained the better practical result. Figure 34 shows the response optimizer prediction trial.

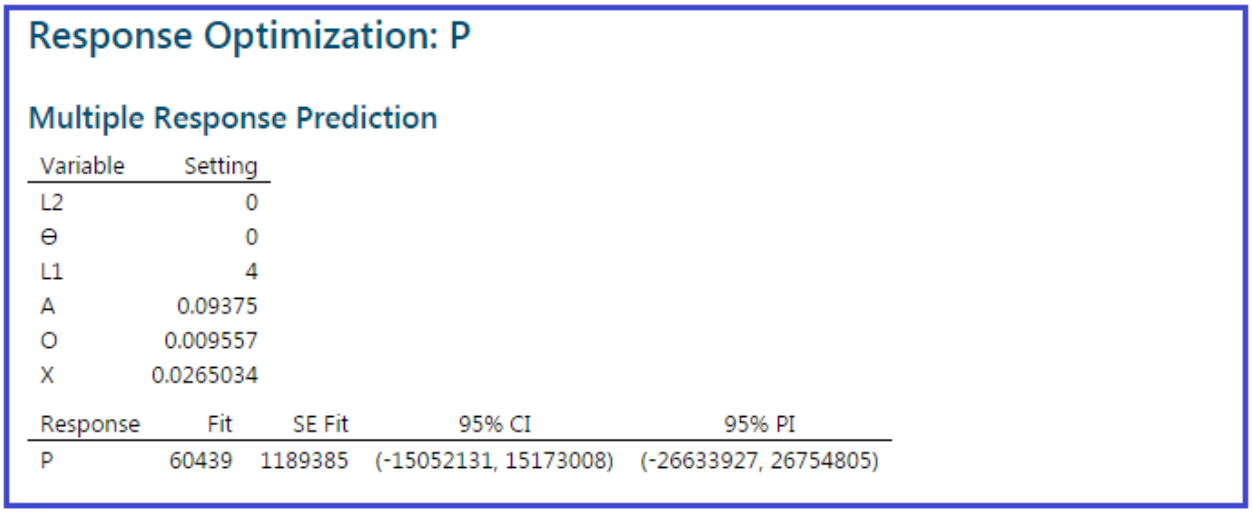

Response Optimization: P

Multiple Response Prediction

Variable	Setting
L2	0
Θ	0
L1	4
A	0.09375
O	0.009557
X	0.0265034

Response	Fit	SE Fit	95% CI	95% PI
P	60439	1189385	(-15052131, 15173008)	(-26633927, 26754805)

FIGURE 34. Response Optimization: P.

The predicted values with 95% confidence Interval were 4, 0.09375, 0.009557, and 0.0265034 for L1, A, O, and X variables, respectively.

In this study, two sets of predicted values for input variables were achieved with two difference L1 values.

4.2 Simulating the Optimum Model

Two optimum models were generated by two sets of variable values. The optimum models were evaluated with the same procedure that earlier applied to each model. Afterward, the comparison between flow pressure drops carried out and the model with less pressure drop was picked as the identified optimum nozzle geometry model in this study.

Table 4 presents the model comparison in details.

TABLE 4. CFD Simulation Results

Model	L1 (in.)	A (in. sq.)	O	E	Θ (degree)	X	L2 (in.)	Pressure Drop (pa)	Volume Average Dynamic Viscosity (Pa.s)
Opt.1	5.94444	0.09375	0	1	0	0	0	7.500377E+04	9.986979 E+02
Opt.2	4	0.09375	0	1	0	0	0	5.852179E+04	9.814309 E+02

As Table 4 presents, the data confirmed that the Model Opt.2 had the less pressure drop and less overall dynamic viscosity. As the result, Model Opt.2 was picked as the optimum presented geometry model of this study. Further, the Model Opt.2 has the least sealant pressure drop among all the main observations, as well.

CHAPTER 5

EXPERIMENTAL PROCEDURE

In this study, experiment was conducted to verify the numerical results. The experiment was accomplished in two stages. First, in order to confirm the Computational Fluid Dynamics (CFD) simulation results and Design of Experiments (DOE) techniques approach, the pressure differential between specific nozzle cross sections was measured for sealant flow inside the nozzle. Second, in order to study the effect of nozzle geometry features on the sealant composition (glass microballoons) and the micro air bubble entrapment/mitigation inside the sealant, Scanning Electron Microscopy (SEM) imaging method was utilized for cured sealant.

5.1 Equipment

5.1.1 Sealant Material

PR-1776M Class B Low Weight fuel tank sealant was studied in this work. Material was purchased from PPG Aerospace company and delivered in Pre-Mixed and Frozen (PMF) form. Figure 35 shows a 6 oz high density natural polyethylene cartridge contains PMF sealant. The sealant technical data sheet will be presented in Appendix A.

FIGURE 35. PMF sealant.

The frozen sealant was defrosted after 30 minutes at ambient temperature. Moreover, in order to experimental study on air bubbles mitigation inside the sealant and to improve the entrapped air bubbles observation, amount of almost 72.5 mm3 air initially was injected into the defrosted sealant before performing the test. Figure 36 shows the air injection by using a food injector syringe.

FIGURE 36. Air injecting into the sealant material before performing the experiment.

5.1.2 Identified Optimum Nozzle Geometry Model.

The presented optimum nozzle geometry model was 3D printed. The model was printed as the module of nozzle attached to the cartridge in order to maintain constant conditions for numerical simulations and experimental conduction, and to decrease the experimental error. Figure 37 shows the 3D printed module.

FIGURE 37. Printed module.

CFD simulations applied to the module of nozzle attached to the cartridge-shaped part. Sealant pressure drop through the cartridge-shaped part was equal for all of the nozzle geometry model modules. Therefore, to decrease the experimental errors and increase the accuracy of verification process, the nozzle was divided into eight equidistant cross sections by drilling the dispensing needles with lure lock connection into the module shell. Pressure was measured at each cross section. In this experiment, the suitable dispensing needle was selected with 0.06 inch inner diameter.

5.1.3 Equipment Setup

The test was conducted on a milling machine (Republic Lagun, model FTV-2F) that two vises were positioned on its table. A mechanized caulking gun, which contains a sealant cartridge, was placed on the first vise and the printed module was placed on the next vise. The caulking gun and the module was attached together and sealed. The rod attached to the collet moving at a constant speed in x direction, provided the constant mass flow inlet, which was set as inlet initial condition in CFD simulations. The rod speed was set to 3.7 $\frac{inch}{min}$. It was calculated based on the mass flow rate of 2.5 grs, module outlet are of 0.0012331 m^2, and sealant density of 1250 $\frac{kg}{m^3}$.

When the sealant flows inside the module, differential pressure between two sections was measured by attaching a handheld digital manometer (HT-18985) to the needles lure locks connection. Since the static pressure was required to be measured and the flow was fairly uniform and stable, insertion tubes were used according to the manometer manual suggestion. In order to avoid pressure disturbance, rest of the dispensing needles were closed by using plastic quick-turn tube coupling lure lock. Figure 38 presents the assembled equipment.

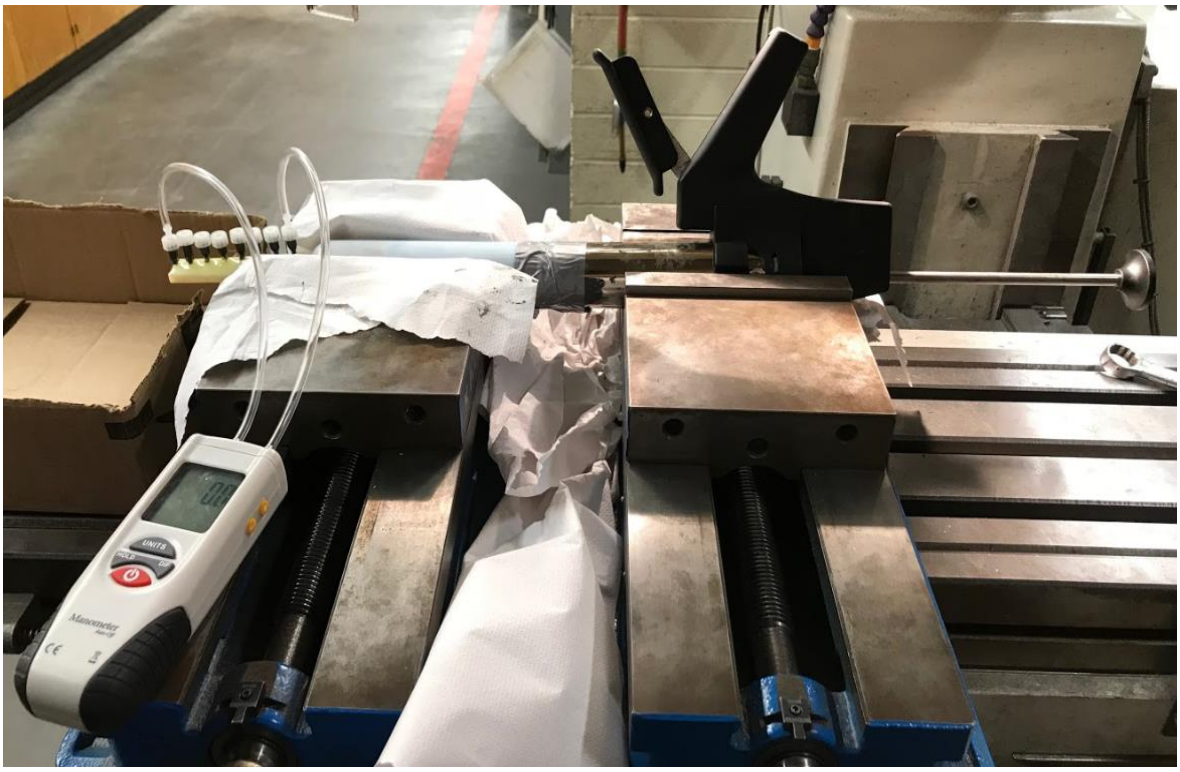

FIGURE 38. Assembled equipment.

5.1.4 Scanning Electron Microscope (SEM)

In order to study the effect of nozzle geometry on the sealant composition (glass microballoons) and the micro air bubbles entrapment mitigation inside the sealant, the Scanning Electron Microscopy (SEM) method using JEOL JSM-7001 microscope was used to observe the condition of hollow glass microballoons on the cured sealant surface.

5.2 Experiment

5.2.1 First Stage

The sealant flowing through the nozzle, digital manometer started measuring the differential pressure. When the material started coming out of the module outlet and the steady state flow was provided, digital manometer showed the stable value for pressure differential. First, the pressure differential of sections 7 and 8 was measured, and then the manometer tubes were switched and attached to the next section probes respectively. Defined sections in

simulation software, in printed module, and in sliced cured sealant inside the module are shown in Figure 39 (a-c).

FIGURE 39. a) Sections in simulation software, b) sections in printed module, c) sections in sliced cure sealant inside the module.

Experimental data, measured pressure differential, will be presented in chapter 6. In addition, results from CFD simulations and experimental data will be compared in details in chapter 6.

5.2.2 Second Stage

In order to study the effect of nozzle geometry on the sealant composition (glass microballoons) and the micro air bubble entrapment mitigation inside the sealant, several cross sections were studied under Scanning Electron Microscope (SEM). Samples of the cured sealant surface in various sections of the nozzle were prepared for SEM analysis. Samples surface were coated by gold to improve the image resolution. SEM images will be presented in chapter 6.

CHAPTER 6

RESULTS, DISCUSSIONS, CONCLUSION, AND FUTURE WORK

6.1 Results and Discussion

In this study, nozzle geometry optimization for shear thinning high viscous fuel tank sealant was studied by investigating the effect of nozzle geometry features on the sealant flow characteristic and behavior. Computational Fluid Dynamics (CFD) simulation was carried out to simulate the sealant flow throughout the nozzle and to study the pressure drop and overall dynamic viscosity behavior of the flow. CFD simulation results were presented in chapter 3 Table 1. Afterwards, the Response Surface Methodology (RSM) was implemented by aid of Design of Experiments (DOE) techniques to identify the optimum mathematical model that leads to minimum sealant pressure drop and minimum overall dynamic viscosity of the sealant throughout the nozzle. In this study the mathematical regression model and its optimum settings were recognized and presented. The optimum regression model and its 3D surface plot are illustrated in Figure 40.

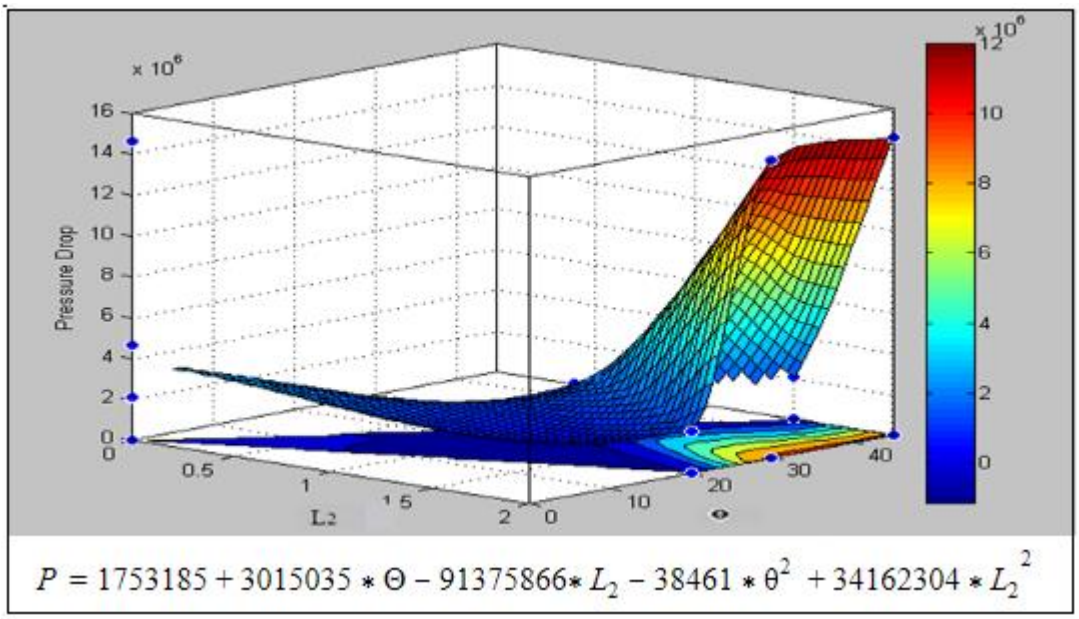

FIGURE 40. Optimum regression nozzle geometry model and 3D surface plot.

In Figure 40, "P" is the sealant pressure drop throughout the nozzle. Moreover, the identified optimum nozzle geometry model was investigated numerically by use of CFD simulations.

In this work, an experiment was conducted to verify the CFD simulation results and DOE optimization approach by experimental data. Table 5 presents the experimental data versus the numerical data derived from CFD simulation software.

TABLE 5. Recorded and Reported Pressure Drop Values

Sections	Experimental Recorded Value (bar)	Numerical Reported Value (pa)	Sections	Experimental Recorded Value (bar)	Numerical Reported Value (pa)
7 to 8	0.070.3%	7.796898e+03	3 to 4	0.030.3%	3.011680e+03
6 to 7	0.0580.3%	5.885094e+03	2 to 3	void	2.635453e+03
5 to 6	0.0440.3%	4.415195e+03	1 to 2	void	2.326891e+03
4 to 5	0.0360.3%	3.569281e+03			

Here the 0.03% presents the digital manometer accuracy.

In Table 5, the experimental data for sections 3 to 1 are not available. The pressure could not be measured at those sections since the sealant material leaked to the needles and clogged them; the experiment could not be repeated due to limited amount of material. Figure 39 shows the comparison graph of CFD simulation results and experimental data.

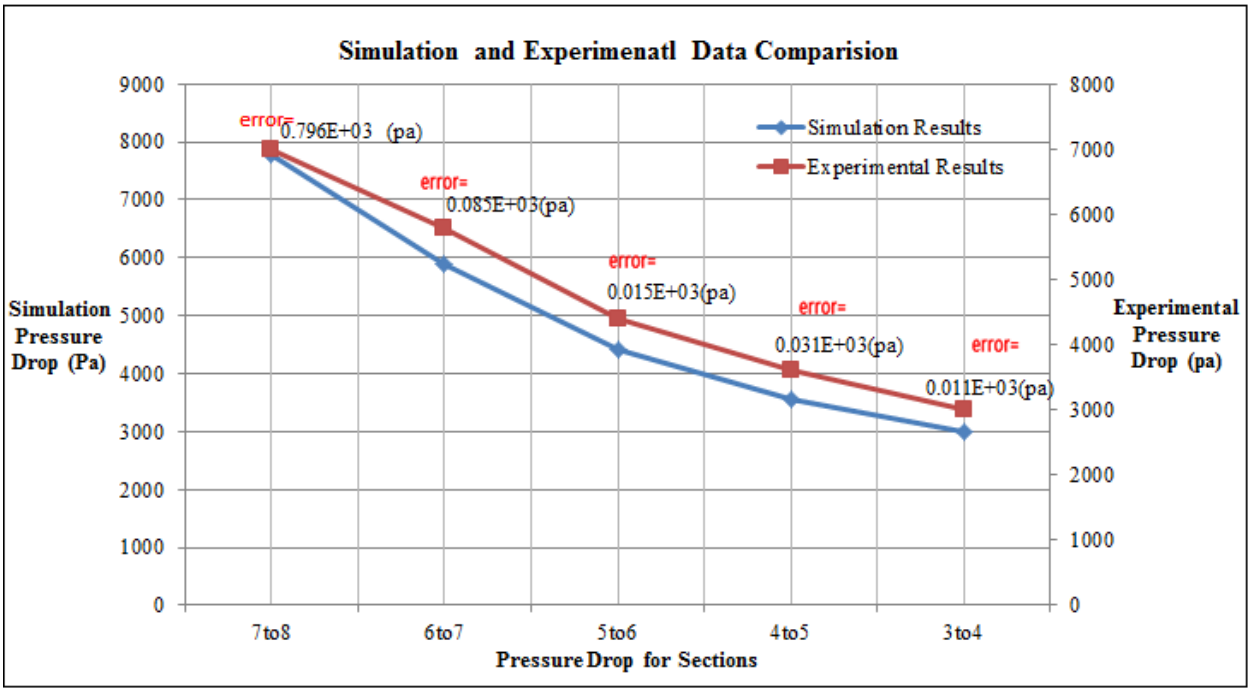

FIGURE 41. Comparison graph to compare experimental data versus simulation results.

As it is shown in Figure 41, CFD simulation and experimental results show the same pattern moving from each point toward the next one, although the error varies between the experimental points and the CFD simulation. The error reaches up to 10% for pressure drop from cross section 7 to 8, which was the first value measured in experiment. This significant error can be the result of transitional flow before it reaches a steady state; however, the errors decrease dramatically for the next measurements.

Further, the experimental study was conducted on mitigating the entrapped air bubbles and breaking the hollow glass microballoons of sealant composition. The module was sliced longitudinally to scan the entrapped air bubbles inside the cured sealant; as the result, Just a small trapped air bubble was observed. Figure 42 shows the sliced sealant and the small air bubble trapped there.

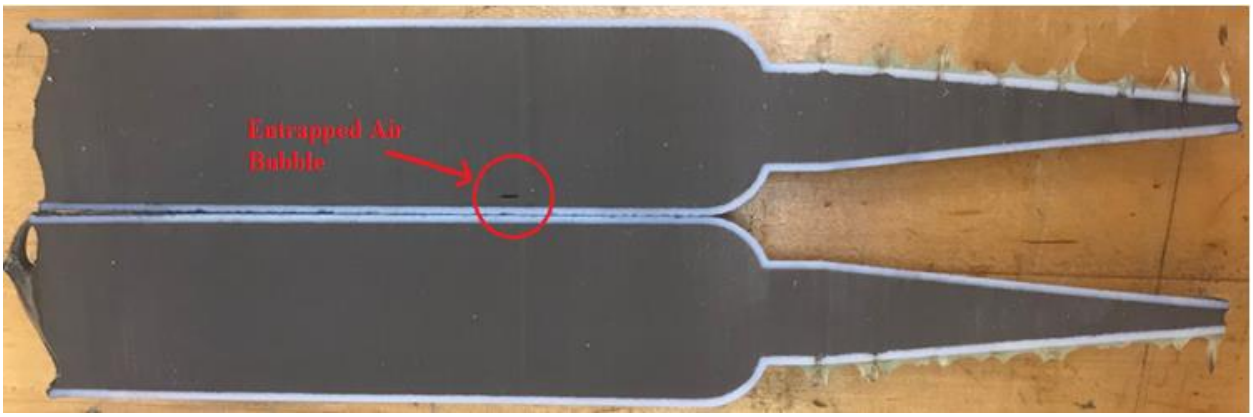

FIGURE 42. The only entrapped air bubble inside the cured sealant.

To improve the air bubble observation in experimental study, almost 72.5 mm^3 amount of air initially was injected into the sealant material before running the experiment. Thus, this small air bubble inside the sealant is simply ignorable and the performance of identified nozzle geometry model in mitigating air bubbles inside the sealant is reasonably confirmed.

Afterwards, experimental study on the sealant composition (glass microballoons) was carried out by using Scanning Electron Microscopy (SEM). Figure 43 illustrates the SEM images taken by JEOL JSM-7001 microscope.

It can be observed in Figure 43(a-d) that the glass microballoons were distributed uniformly on the cross section surface. Although no ruptured or crushed glass microballoon can be observed in Figure 43, some cavities are observed on cross section surface that may pertain to the segments in which glass microballoons were pinned before the sample was sliced. It can be concluded form Figure 43 observations that the presented nozzle geometry model in this study does not destroy the glass microballoons structure in the sealant composite.

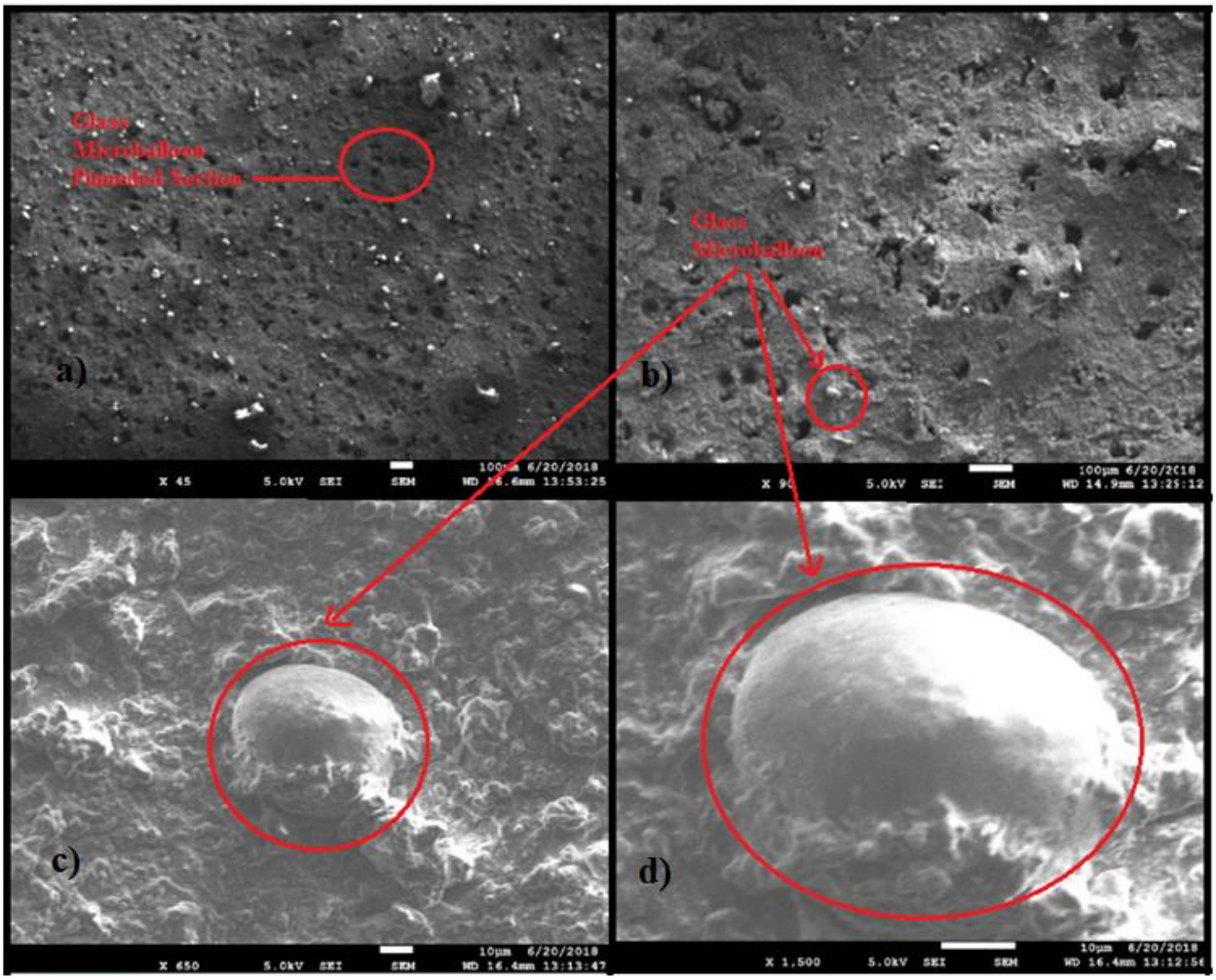

FIGURE 43. a,b) SEM images at magnification 100µm. c,d) SEM image at magnification 10µm.

6.2 Conclusion

In this study, the effect of nozzle geometrical features on the shear thinning non-Newtonian high viscous fuel tank sealant (PR-1776M Class B Low Weight fuel tank sealant) was investigated. Computational Fluid Dynamics (CFD) simulations were carried out to numerically study the sealant flow characterization and behavior using STAR-CCM+ software. In this study, high viscous shear thinning sealant material was modeled properly by generalized Newtonian Carreau-Yasuda model for the first time, when it was used to be modeled by generalized Newtonian power law model. The compatibility of the Carreau-Yasuda model with

the high viscous shear thinning sealant flow behavior was confirmed. Afterwards, Response Surface Methodology (RSM) was implemented by the aid of Design of Experiments (DOE) techniques, to develop the optimized mathematical model based on the collected data from numerical results.

Afterward, a 3D model of the optimized nozzle geometry model was built to conduct the experiment with the sealant material and to verify the results of the numerical investigations. Strength of the Computational Fluid Dynamics (CFD) simulations and Design of Experiments (DOE) approach were demonstrated by experimental data validation, although both the experimental measurements and software simulations are not free from errors.

The geometry optimization pattern that was conducted in this study is a valuable pattern for geometry optimization and design of the fluid systems that deal with non-Newtonian fluids. In addition, the identified nozzle geometry model in this work can be considered an applicable sealant nozzle template for the aerospace industries equipment manufacturers.

6.3 Future Work

In the following we propose recommendations in order to further develop this study:

The sealant material with high viscous shear thinning non-Newtonian properties was properly modeled by generalized Newtonian Carreau-Yasuda model. This model contains temperature shift factor to adjust viscosity with temperature. In this study, the sealant was assumed isothermal with temperature shift factor of 1. For further study, it is required to investigate the effect of temperature on viscosity behavior of sealant by applying the proper temperature shift factor.

In this study, the performance of identified nozzle geometry model in mitigating air bubbles inside the sealant was studied and the result was satisfying. For further development in

sealant air bubbles mitigation area, a research study can be conducted to degassing the sealant by nozzle geometry optimization.

In this research study, geometry optimization of the sealant nozzle was carried out based on the general sealant nozzle applications. Nozzle geometry optimization can be performed individually for special sealant nozzle applications such as for applying overlapping or fillet seals, for applying fay surface seals, for applying hard-to-reach applications seals, and to deposit a precise amount of sealant; subsequently, more geometrical features required to be considered and studied [12].

In the experimental procedure, more material source should be utilized to conduct the real steady state flow. Moreover, the validation experiment can be performed several times to collect more accurate experimental data.

APPENDICES

APPENDIX A

PR-1776M CLASS B LOW WEIGHT FUEL TANK SEALANT TECHNICAL DATA SHEET

PPG Aerospace
PRC-DeSoto

TECHNICAL DATA

PR-1776M Class B Low Weight Fuel Tank Sealant

Description

PR-1776M Class B is a low density, high temperature aircraft integral fuel tank sealant. It has a service temperature range from -65°F (-54°C) to 250°F (121°C), with very limited excursions up to 360°F (182°C). This material is designed for fillet sealing of fuel tanks and other aircraft fuselage sealing applications. It offers as much as a twenty percent weight savings, per unit volume, over traditional sealants used for these purposes. The cured sealant maintains excellent elastomeric properties after prolonged exposure to aircraft fuels both jet fuel and aviation gas, and will resist limited contact to diphosphate ester based hydraulic fluids.

PR-1776M Class B is a two-part, manganese dioxide cured Permapol® P-5 modified polysulfide. The uncured material is a low sag, thixotropic paste suitable for application by extrusion gun or spatula. It cures at room temperature to form a resilient sealant having excellent adhesion to common aircraft substrates.

PR-1776M Class B is designed to be a direct replacement for PR-1776 Class B.

The following tests are in accordance with AMS-3281 and BMS 5-45 specification test methods.

Application Properties (Typical)

Color	
Part A	Black
Part B	Off white
Mixed	Dark brown
Mixing ratio, By weight	Part A:Part B
B-1/2	12:100
B-2	10:100
Base viscosity (Brookfield #7 @ 2 rpm), Poise (Pa-s)	11,100 (1,100)

Slump, inches (mm)

	Initial	50 Minutes	90 Minutes
B-1/2	0.20 (5.08)	———	———
B-2	0.15 (3.81)	0.15 (3.81)	0.15 (3.81)
	Initial	3 Hours	5.5 Hours
B-6	.10 (2.54)	.10 (2.54)	.10 (2.54)

Application life and cure time @ 77°F (25°C), 50% RH

	Application life (hours)	Tack free time (hours)	Cure time to 30 A Durometer (hours)
B-1/2	1/2	<8	12
B-2	2	<16	24
B-4	4	<24	48
B-6	6	<30	80

Performance Properties (Typical)

Cured 14 days @ 77°F (25°C), 50% RH	
Cured specific gravity	1.29
Nonvolatile content, %	94
Ultimate cure hardness, Durometer A	50
Peel strength, pli (N/25 mm), 100% cohesion	
JRF immersion with 0.25 inch (6.35mm) layer of distilled H_2O, 7 days @ 140°F (60°C)	
MIL-C-5541 (Alodine Aluminum)	41 (180)
MIL-T-9046 Type I (Titanium Comp 'B')	36 (158)
BMS 10-20 Type II Grade A (Epoxy primer)	42 (184)
BMS 10-20 Type II Grade D (Epoxy primer)	42 (184)
BMS 10-20 Type II (B/A) (Epoxy primer)	35 (154)
3% NaCl-H_2O immersion with 1.0 inch (25.4mm) layer of JRF, 7 days @ 140°F (60°C)	
MIL-C-5541 (Alodine Aluminum)	34 (149)
MIL-T-9046 Type I (Titanium Comp 'B')	40 (176)
BMS 10-20 Type II Grade A (Epoxy primer)	36 (158)
BMS 10-20 Type II Grade D (Epoxy primer)	37 (162)
BMS 10-20 Type II (B/A) (Epoxy primer)	34 (149)
AMS 2629 Type I Fuel immersion, 7 days @ 140°F (60°C)	
AMS 2471 (Anodized aluminum)	25 (110)
AMS 5516 (Stainless steel*)	26 (114)
MIL-C-27725 (IFT coating)	22 (97)
AMS 2629 Type I Fuel immersion with 3% NaCl-H_2O, 7 days @ 140°F (60°C)	
AMS 2471 (Anodized aluminum)	32 (141)
AMS 5516 (Stainless steel*)	33 (145)
MIL-C-27725 (IFT coating)	28 (123)
3% NaCl-H_2O immersion, 7 days @ 140°F (60°C)	
MIL-PRF-85582 (Epoxy primer*)	33 (145)
MIL-PRF-85285 (Urethane top coat*)	34 (149)
*Primed with PR-148 adhesion promoter.	
Tensile strength, psi (KPa) Standard cure, 14 days @ 77°F (25°C), 50% RH	263 (1812)
7 days immersion in JRF @ 140°F (60°C)	269 (1853)
Elongation, % Standard cure, 14 days @ 77°F (25°C), 50% RH	366
7 days immersion in JRF @ 140°F (60°C)	439
Low temperature flexibility @ -65°F (-54°C) - No cracking, checking or loss of adhesion.	
Resistance to hydrocarbons - 7 days @ 140°F (60°C)immersed in JRF	
Weight loss, %	4.7

Where Smart Solutions Take Flight®

APPENDIX B

SEMCO SPECIALTY APPLICATION NOZZLES

Semco® Specialty Application Nozzles

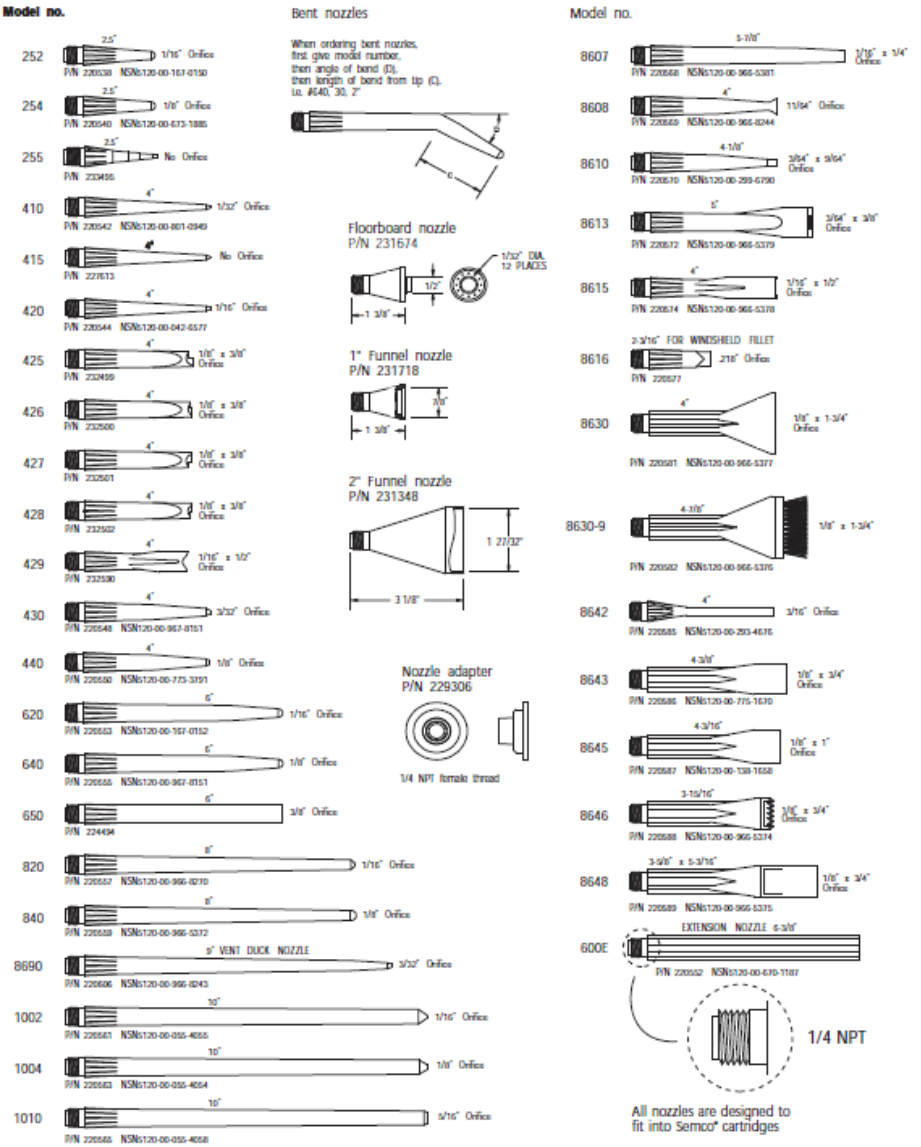

Printed in the U.S.A

PRC-DeSoto International, Inc.
12780 San Fernando Road
Sylmar, CA 91342
Telephone (818) 362-6711
Toll Free (800) AEROMIX
www.semcopackaging.com

Issue Date: 06/12
Supersedes: 11/02
Lit: 0625

APPENDIX C

CFD SIMULATIONS SCENES: PRESSURE DISTRIBUTIONS, VELOCITY VECTORS, DYNAMIC VISCOSITY DISTRIBUTIONS, FLOW STREAMLINES

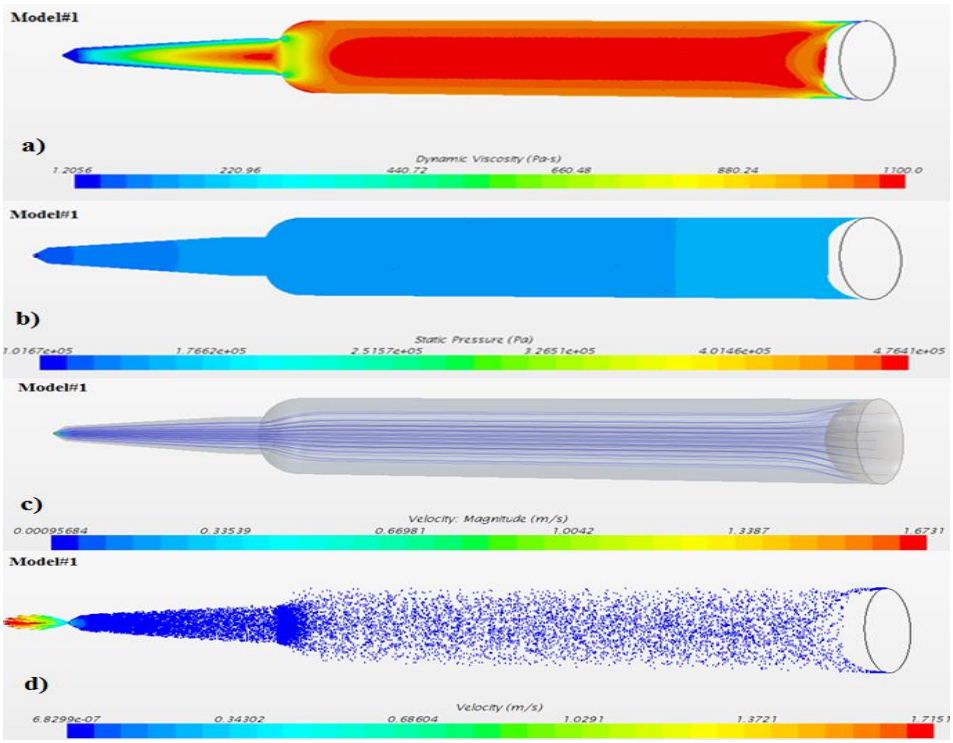

FIGURE 44. Model #1 CFD simulation scenes.

Figure 44 (a – d) shows dynamic viscosity distribution, pressure distribution, flow streamlines, and velocity vectors scenes for CFD simulation of Model #1.

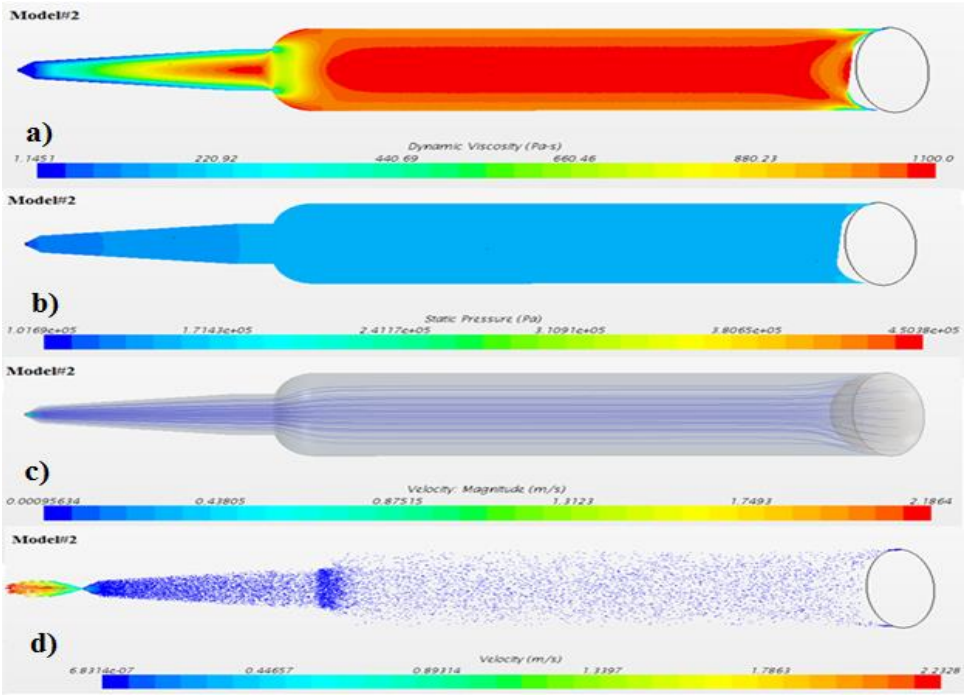

FIGURE 45. Model #2 CFD simulation scenes.

Figure 45 (a – d) shows dynamic viscosity distribution, pressure distribution, flow streamlines, and velocity vectors scenes for CFD simulation of Model #2.

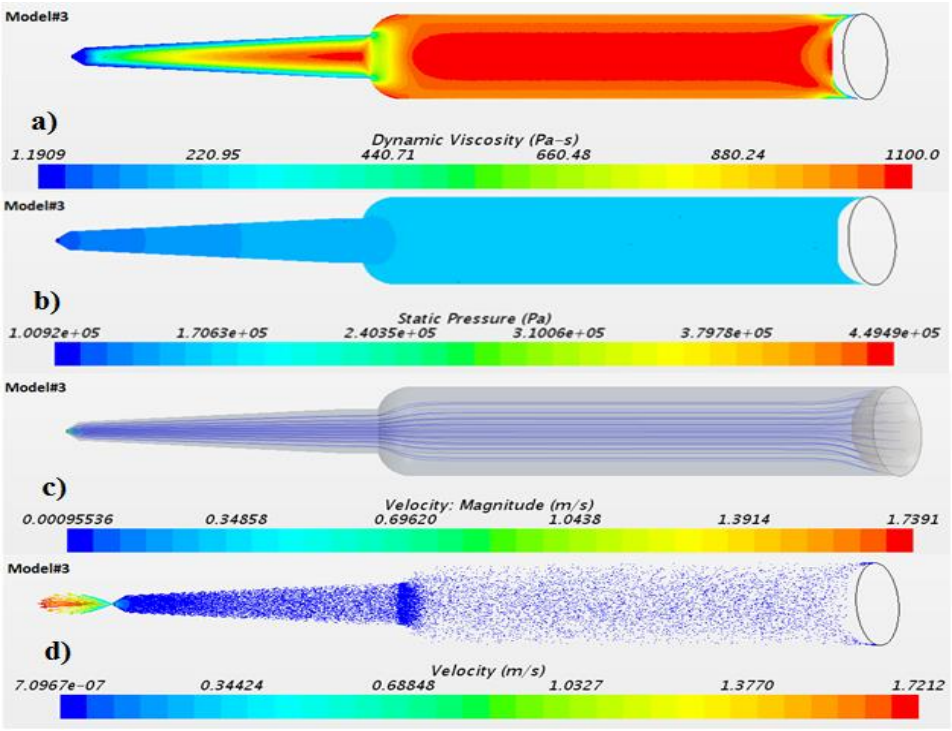

FIGURE 46. Model #3 CFD simulation scenes.

Figure 46 (a – d) shows dynamic viscosity distribution, pressure distribution, flow streamlines, and velocity vectors scenes for CFD simulation of Model #3.

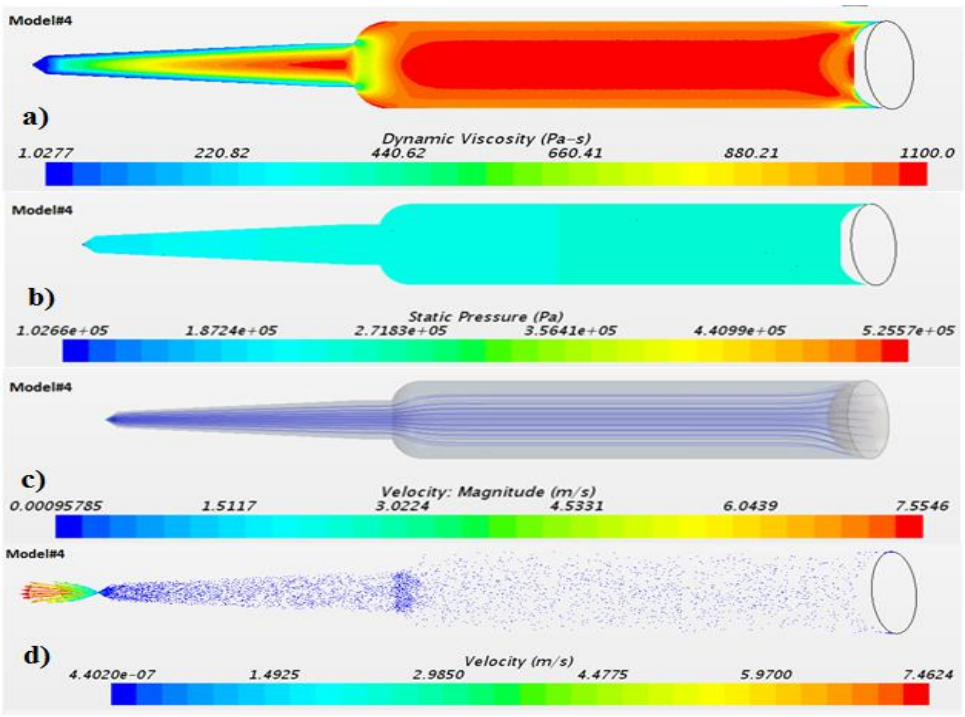

FIGURE 47. Model #4 CFD simulation scenes.

Figure 47 (a – d) shows dynamic viscosity distribution, pressure distribution, flow streamlines, and velocity vectors scenes for CFD simulation of Model #4.

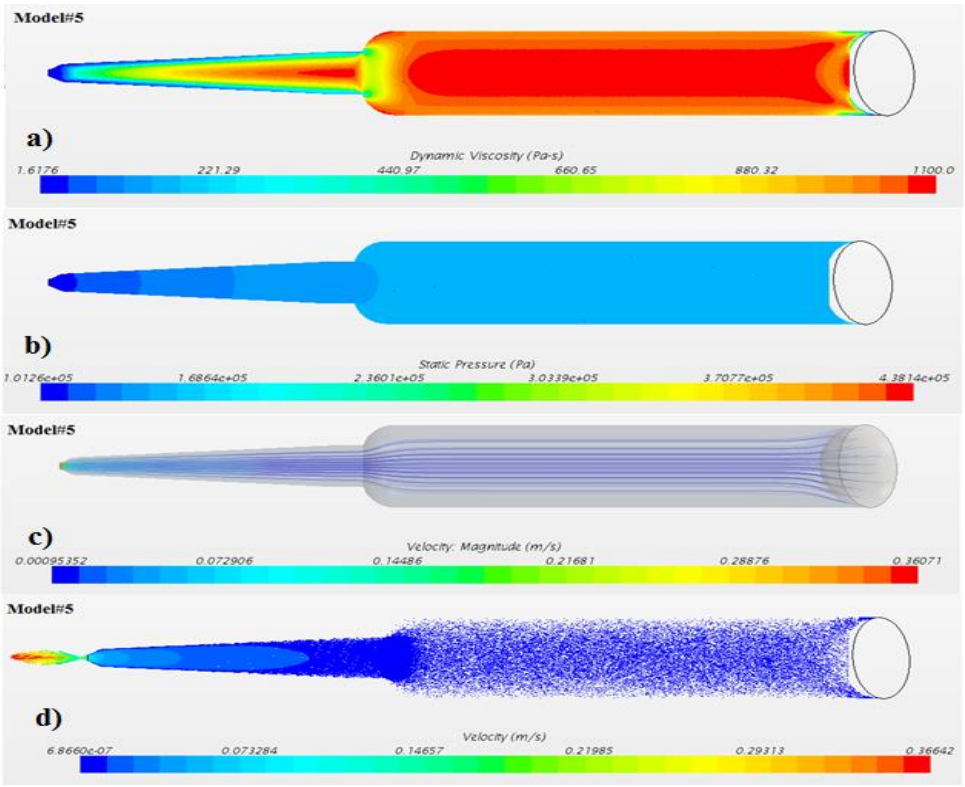

FIGURE 48. Model #5 CFD simulation scenes.

Figure 48 (a – d) shows dynamic viscosity distribution, pressure distribution, flow streamlines, and velocity vectors scenes for CFD simulation of Model #5.

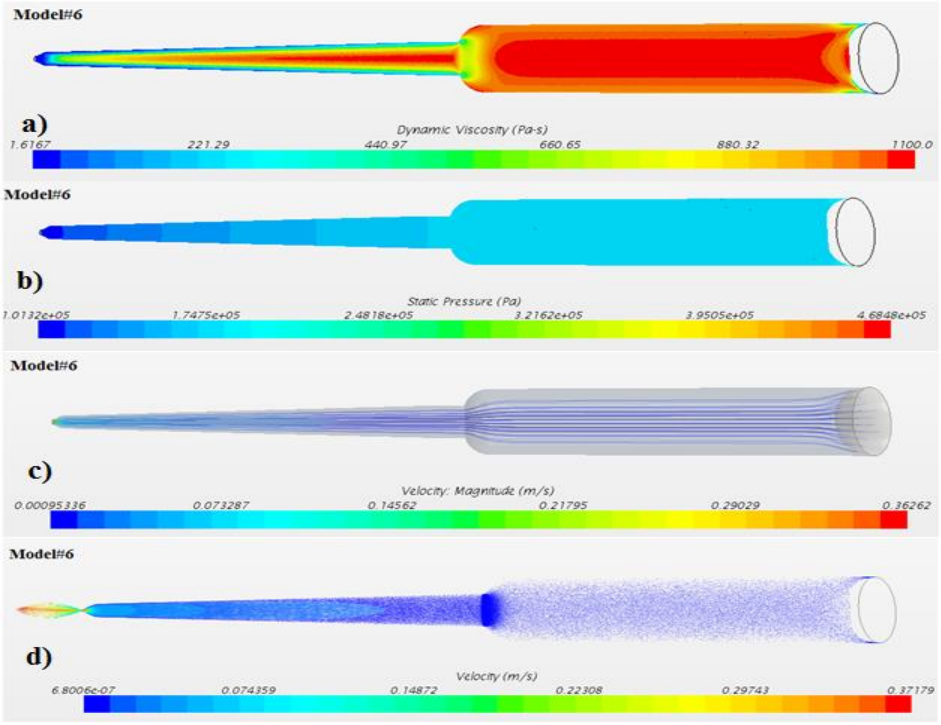

FIGURE 49. Model #6 CFD simulation scenes.

Figure 49 (a – d) shows dynamic viscosity distribution, pressure distribution, flow streamlines, and velocity vectors scenes for CFD simulation of Model #6.

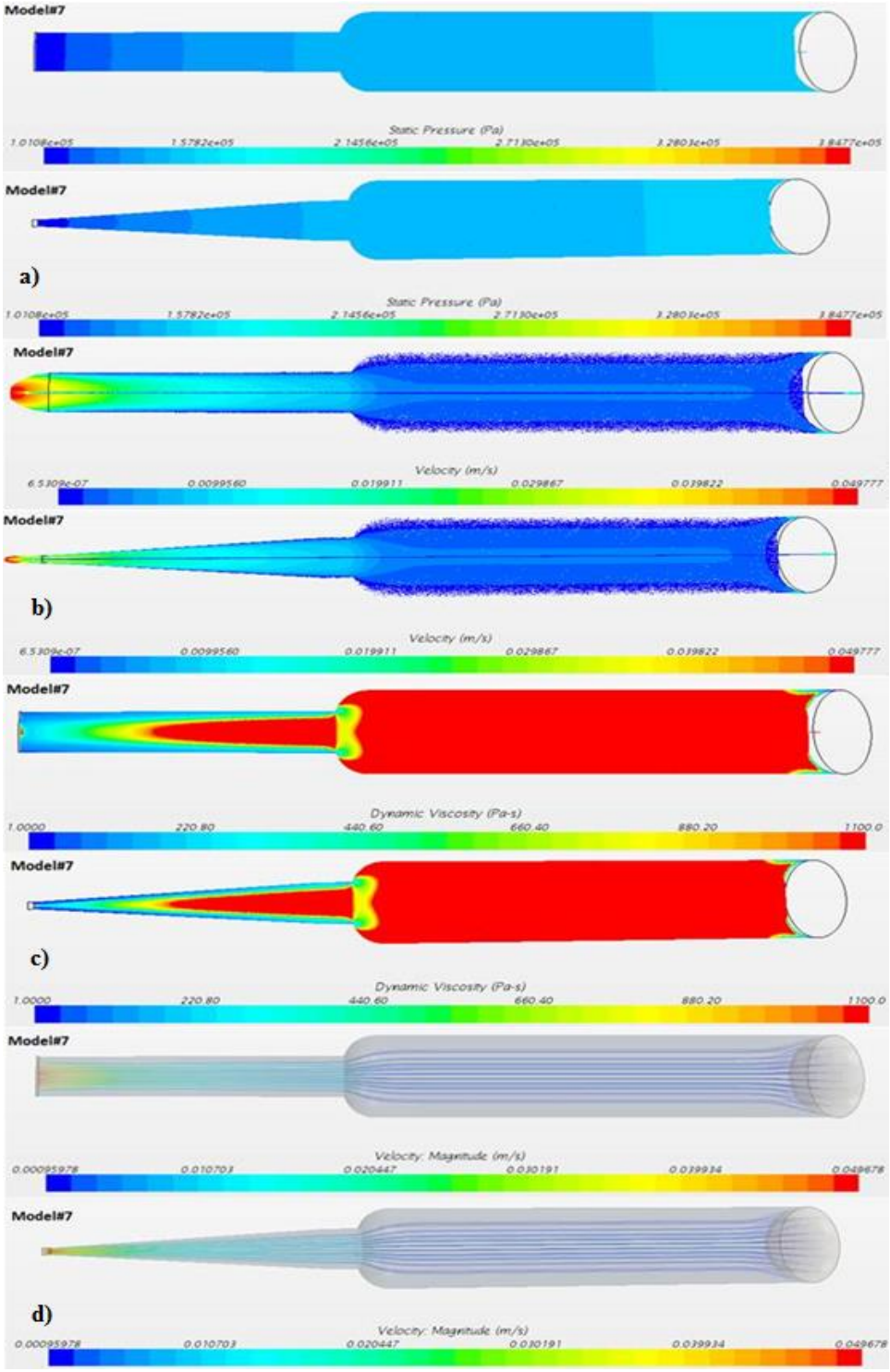

FIGURE 50. Model #7 CFD simulation scenes.

Figure 50 (a – d) shows pressure distribution, velocity vectors, dynamic viscosity distribution, and flow streamlines scenes for CFD simulation of Model #7.

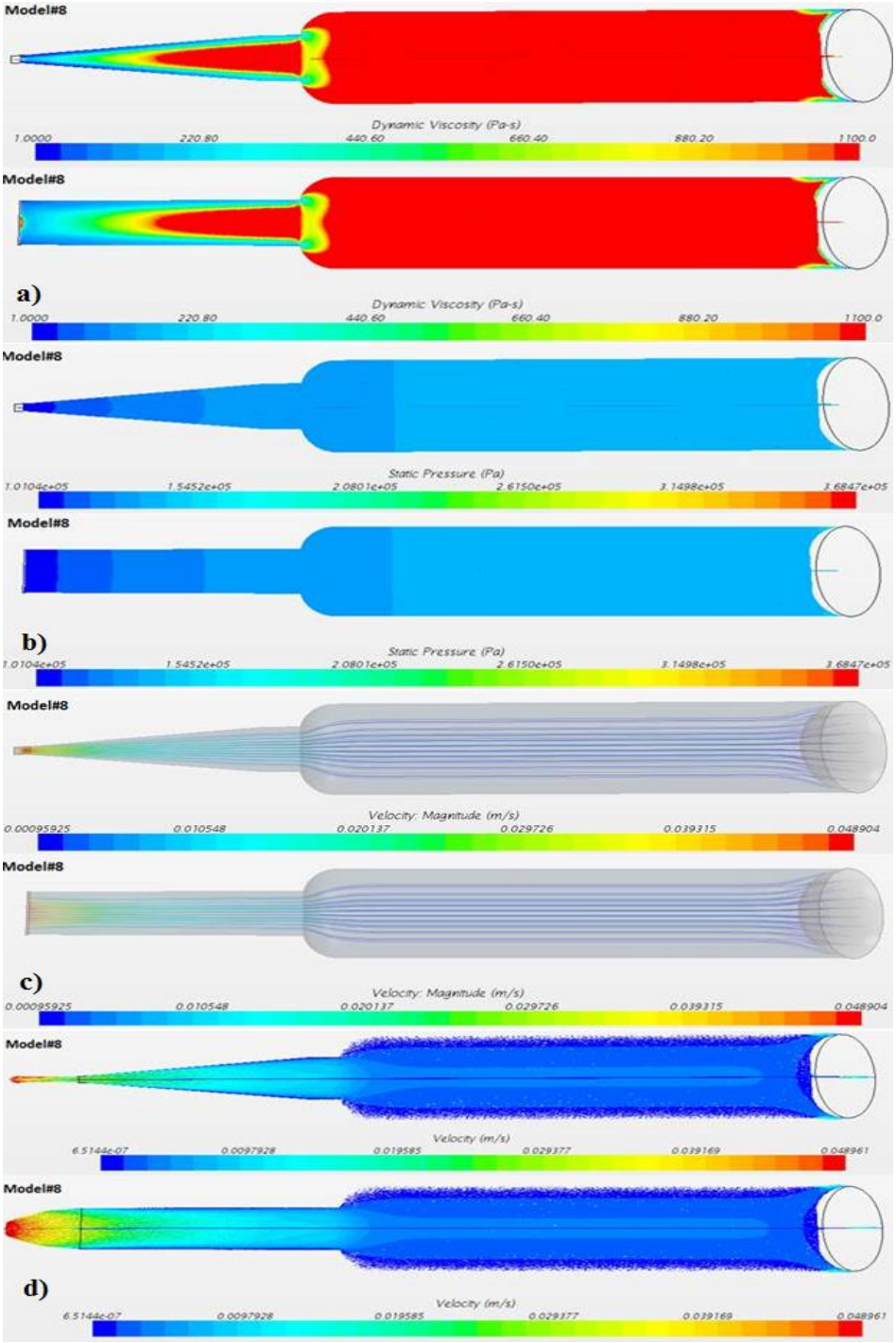

FIGURE 51. Model #8 CFD simulation scenes.

Figure 51 (a – d) shows dynamic viscosity distribution, pressure distribution, flow streamlines, and velocity vectors scenes for CFD simulation of Model #8.

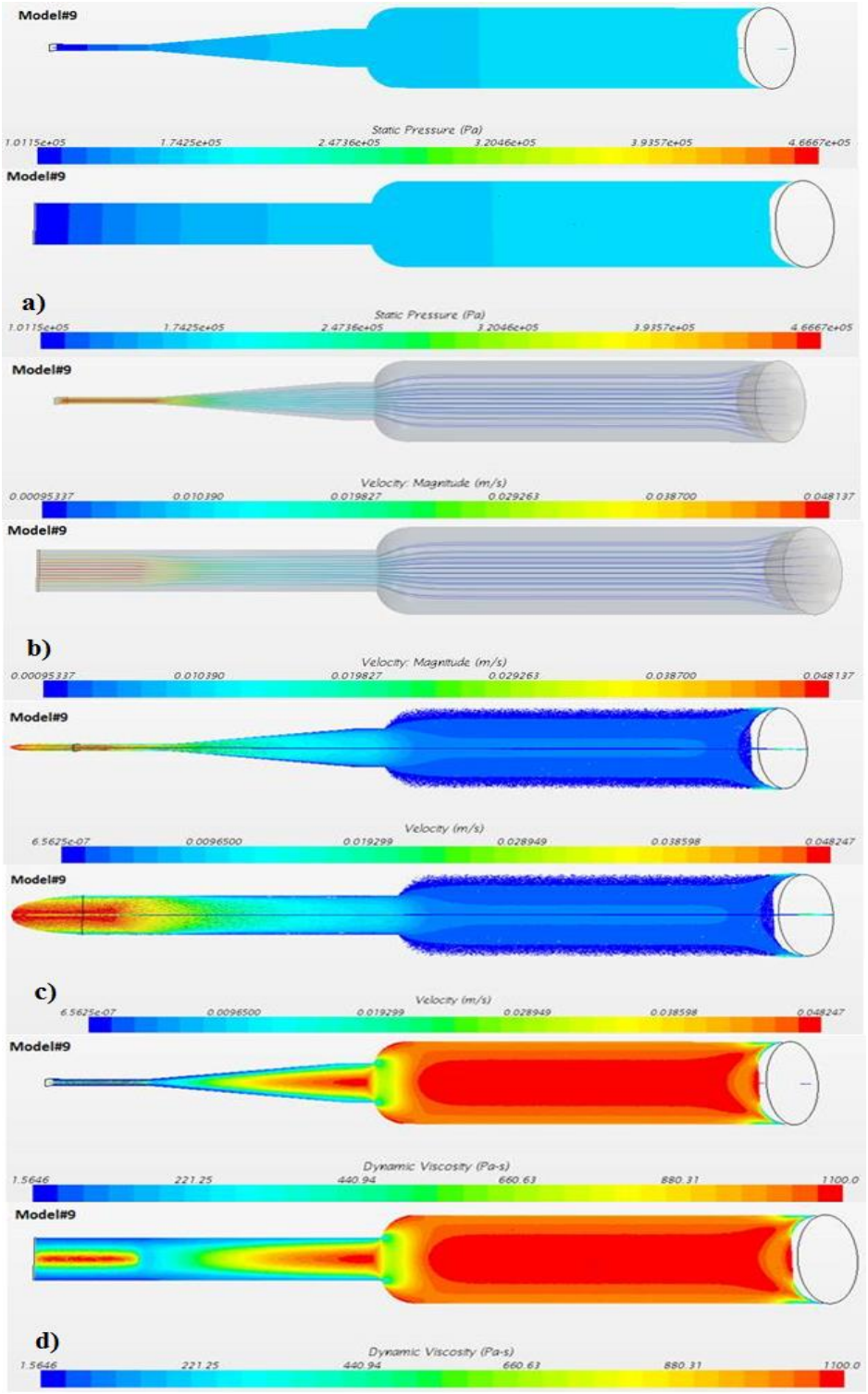

FIGURE 52. Model #9 CFD simulation scenes.

Figure 52 (a – d) shows pressure distribution, flow streamlines, velocity vectors, and dynamic viscosity distribution scenes for CFD simulation of Model #9.

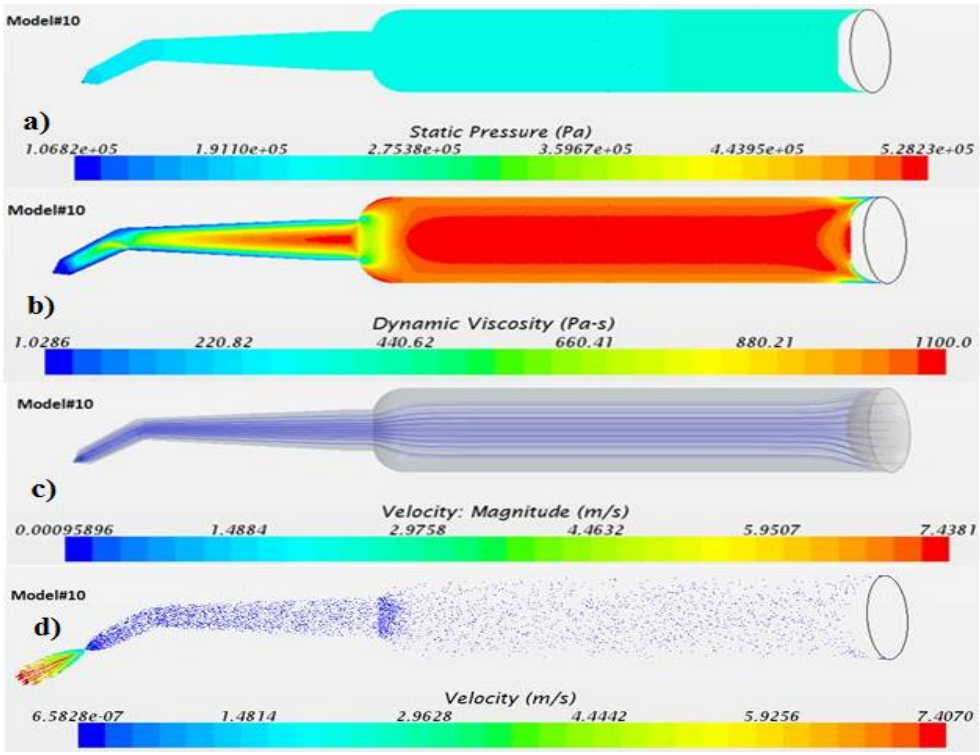

FIGURE 53. Model #10 CFD simulation scenes.

Figure 53 (a – d) shows pressure distribution, dynamic viscosity distribution, flow streamlines, and velocity vectors scenes for CFD simulation of Model #10.

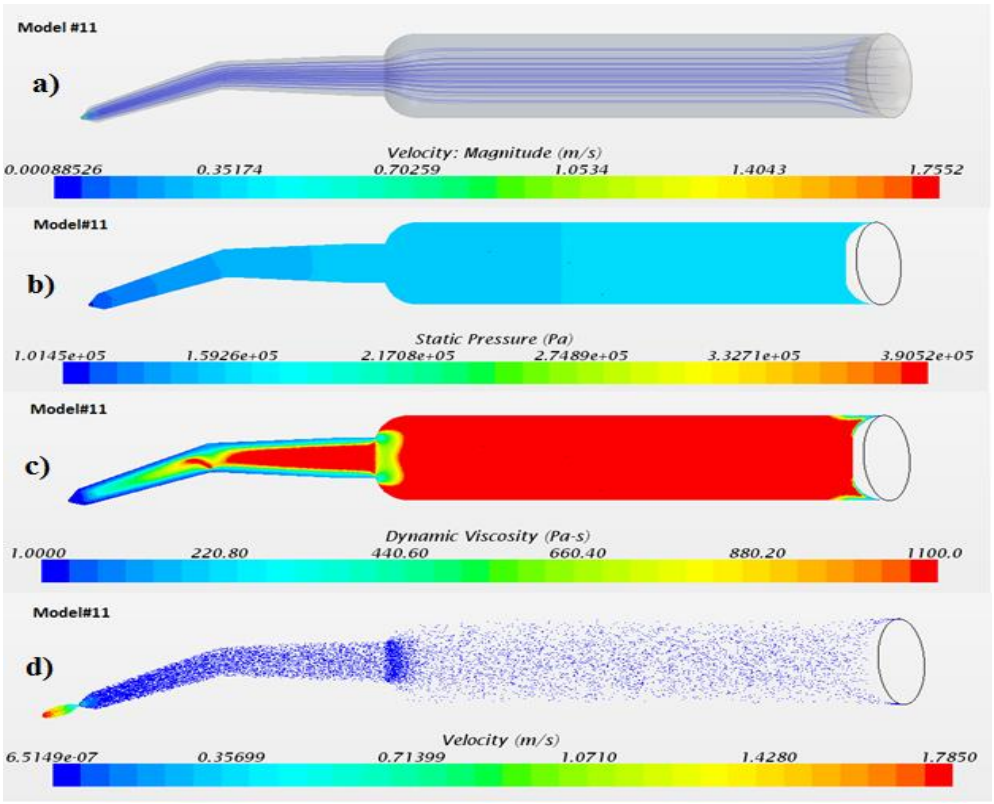

FIGURE 54. Model #11 CFD simulation scenes.

Figure 54 (a – d) shows pressure distribution, dynamic viscosity distribution, flow streamlines, and velocity vectors scenes for CFD simulation of Model #11.

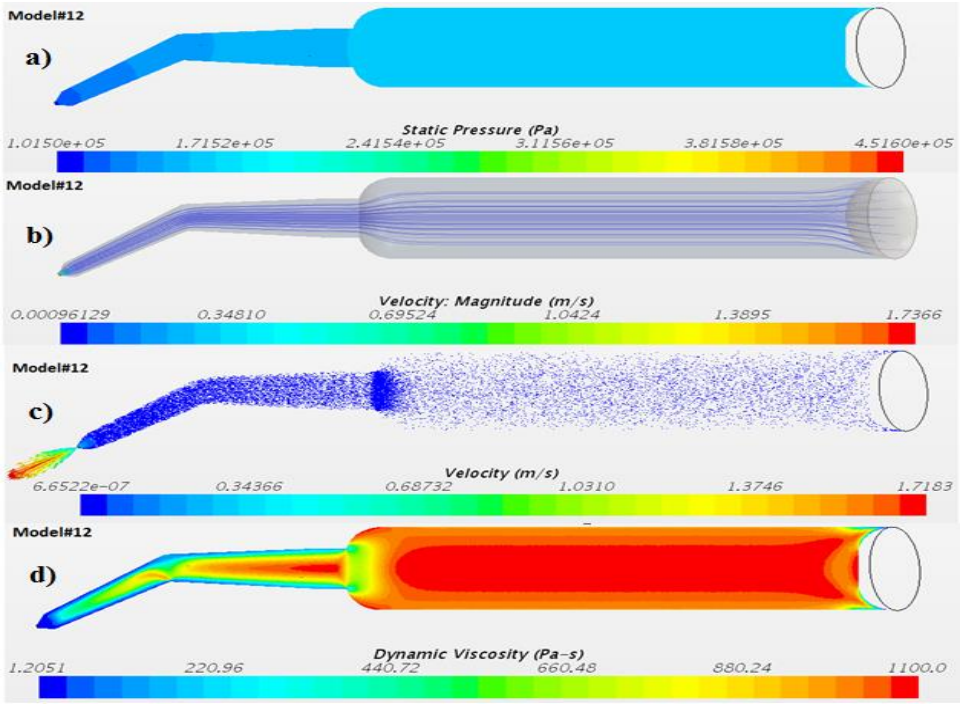

FIGURE 55. Model #12 CFD simulation scenes.

Figure 55 (a – d) shows pressure distribution, flow streamlines, velocity vectors, and dynamic viscosity distribution scenes for CFD simulation of Model #12.

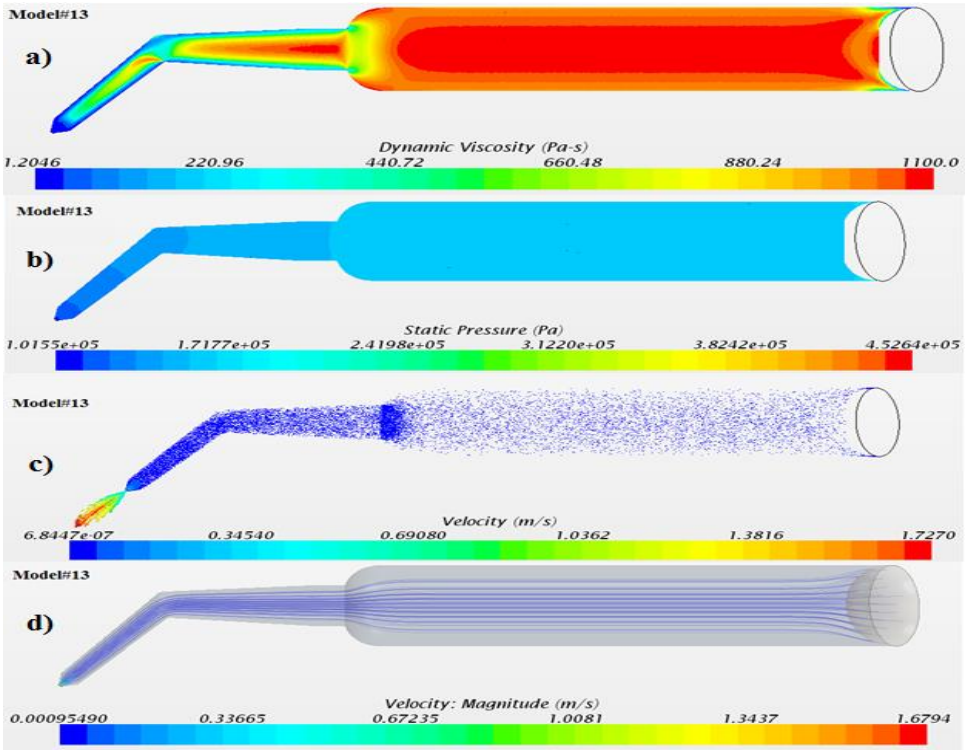

FIGURE 56. Model #13 CFD simulation scenes.

Figure 56 (a – d) shows dynamic viscosity distribution, pressure distribution, velocity vectors, and flow streamlines scenes for CFD simulation of Model #13.

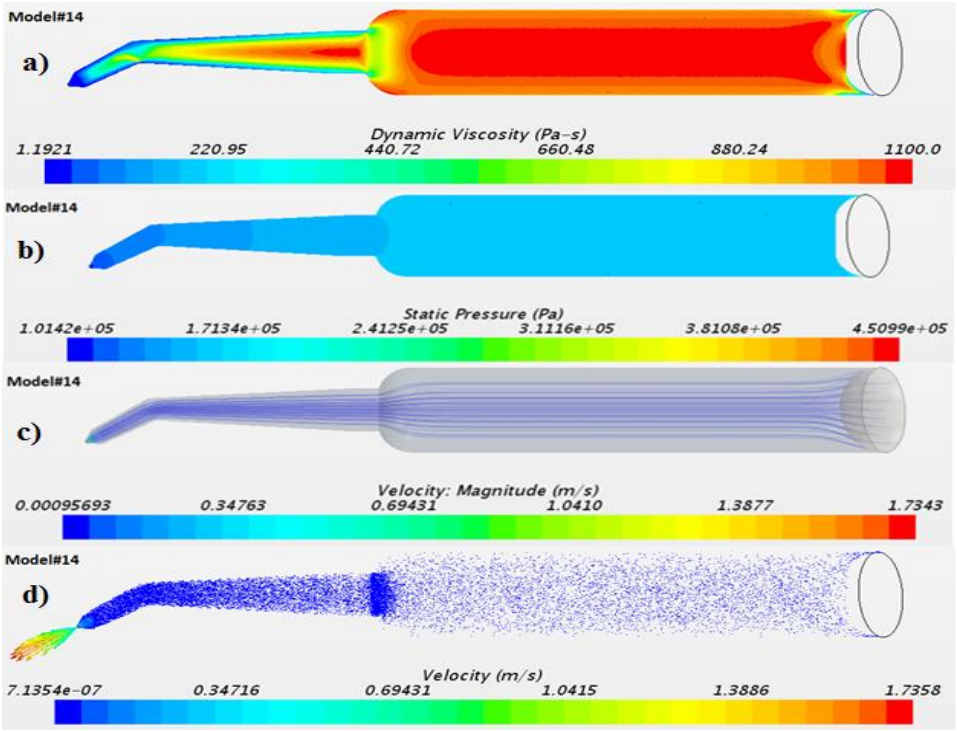

FIGURE 57. Model #14 CFD simulation scenes.

Figure 57 (a – d) shows dynamic viscosity distribution, pressure distribution, flow streamlines, and velocity vectors scenes for CFD simulation of Model #14.

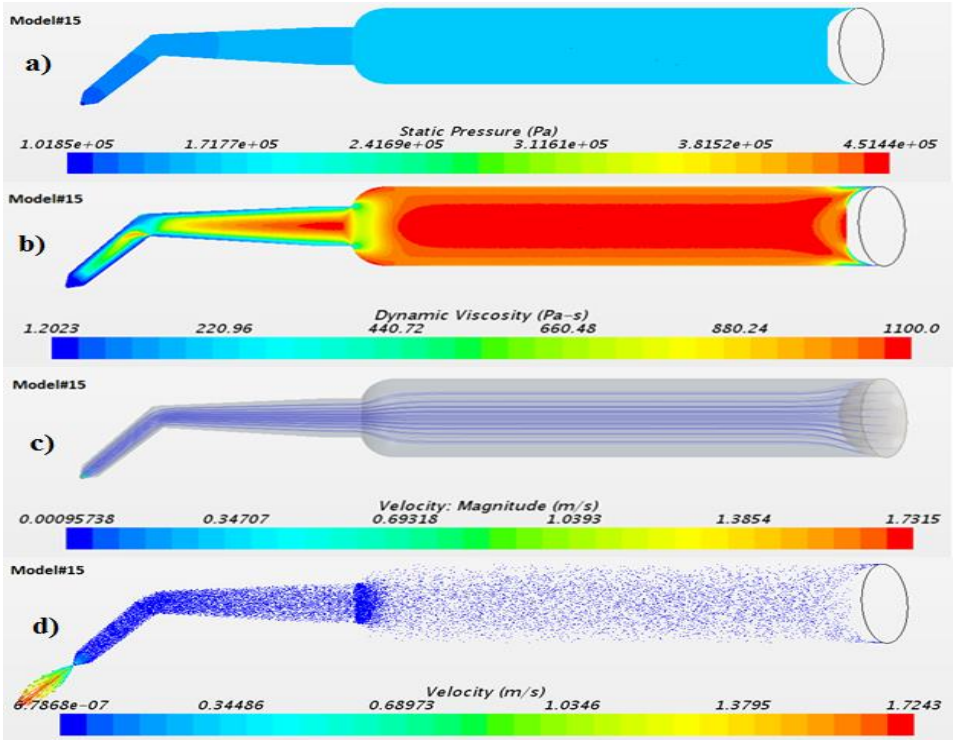

FIGURE 58. Model #15 CFD simulation scenes.

Figure 58 (a – d) shows pressure distribution, dynamic viscosity distribution, flow streamlines, and velocity vectors scenes for CFD simulation of Model #15.

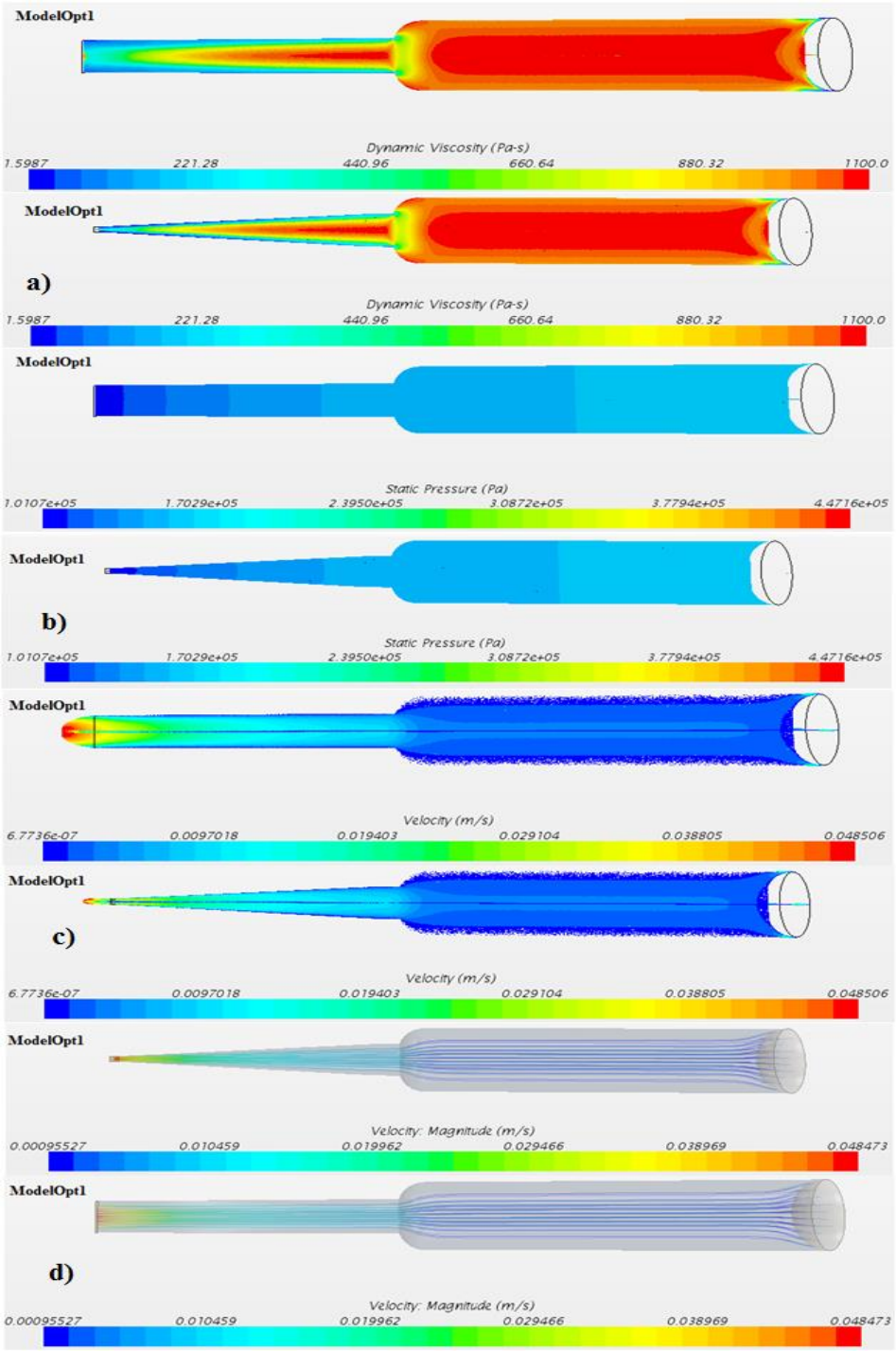

FIGURE 59. Model Opt1 CFD simulation scenes.

Figure 59 (a – d) shows pressure distribution, dynamic viscosity distribution, flow streamlines, and velocity vectors scenes for CFD simulation of ModelOpt1.

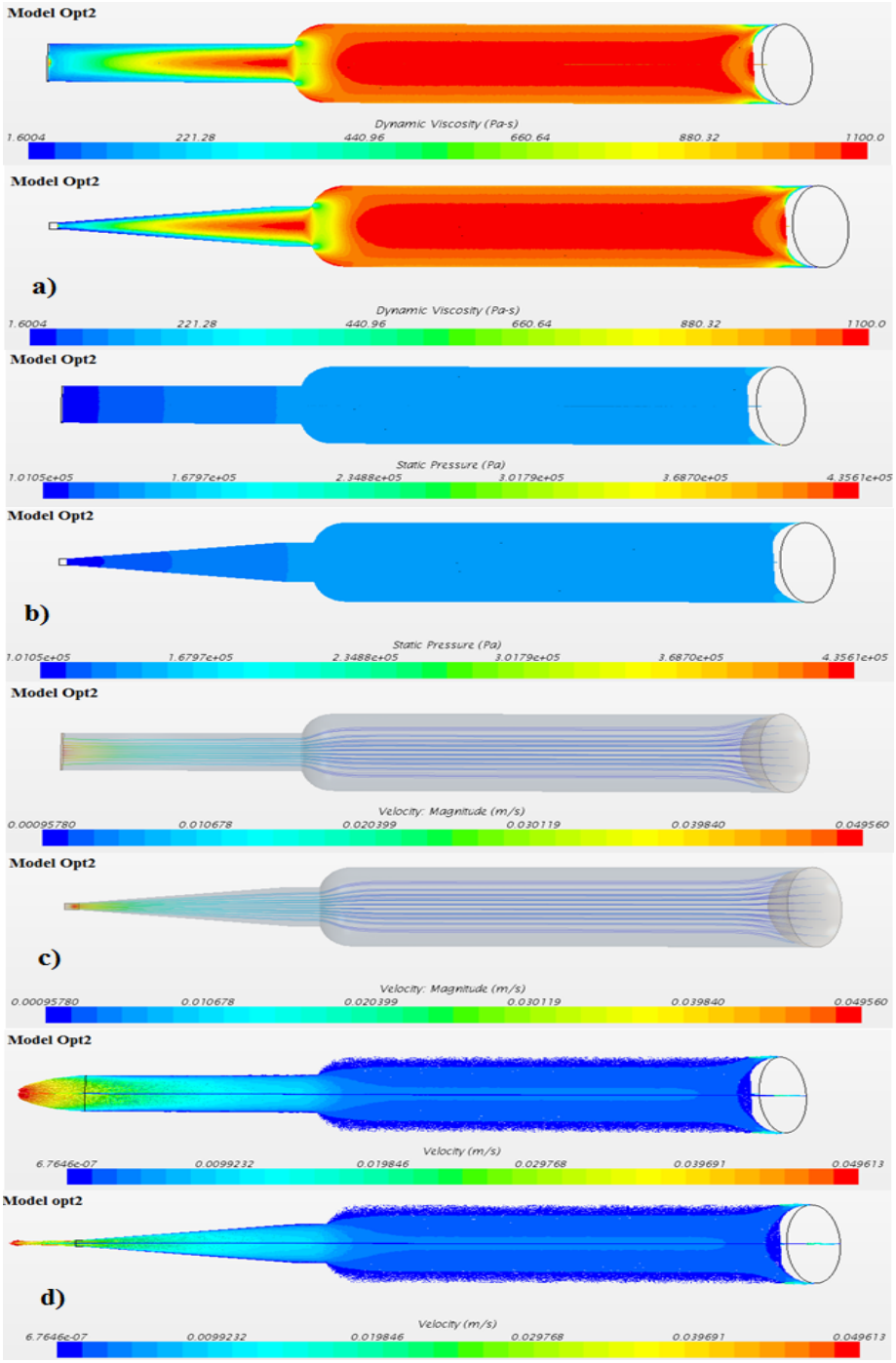

FIGURE 60. Model Opt2 CFD simulation scenes.

Figure 60 (a – d) shows dynamic viscosity distribution, pressure distribution, flow streamlines, and velocity vectors scenes for CFD simulation of ModelOpt2.

APPENDIX D

DESIGN OF EXPERIMENTS TABLES

Regression Analysis: P versus L1, A , O , E , Θ , X , L2

Stepwise Selection of Terms

α to enter = 0.3, α to remove = 0.3
The stepwise procedure added terms during the procedure in order to maintain a hierarchical model at each step.
Beginning with step 2, the model may not be hierarchical because some required terms are impossible to estimate.

Analysis of Variance

Source	DF	Adj SS	Adj MS	F-Value	P-Value
Regression	3	2.27083E+14	7.56944E+13	5.87	0.012
Θ *Θ	1	1.39475E+14	1.39475E+14	10.81	0.007
L2*L2	1	1.06199E+14	1.06199E+14	8.23	0.015
Θ *L2	1	1.41939E+14	1.41939E+14	11.01	0.007
Error	11	1.41870E+14	1.28973E+13		
Total	14	3.68953E+14			

Model Summary

S	R-sq	R-sq(adj)	R-sq(pred)
3591277	61.55%	51.06%	43.01%

Coefficients

Term	Coef	SE Coef	T-Value	P-Value	VIF
Constant	1722849	1164867	1.48	0.167	
Θ *Θ	-39694	12071	-3.29	0.007	83.40
L2*L2	-11800384	4112292	-2.87	0.015	49.12
Θ *L2	1546771	466256	3.32	0.007	218.04

Regression Equation

P = 1722849 - 39694 Θ *Θ - 11800384 L2*L2 + 1546771 Θ *L2

Fits and Diagnostics for Unusual Observations

Obs	P	Fit	Resid	Std Resid	
3	12629200	1722849	10906351	3.21	R
11	72800	514568	-441767	-0.39	X

R Large residual
X Unusual X

FIGURE 61. DOE procedure first try.

Regression Analysis: P versus L2, Θ

The following terms cannot be estimated and were removed:
L2*Θ

Analysis of Variance

Source	DF	Adj SS	Adj MS	F-Value	P-Value
Regression	4	2.27240E+14	5.68100E+13	4.01	0.034
Θ	1	8.51863E+13	8.51863E+13	6.01	0.034
L2	1	1.13255E+14	1.13255E+14	7.99	0.018
Θ*Θ	1	7.04891E+13	7.04891E+13	4.97	0.050
L2*L2	1	1.29867E+14	1.29867E+14	9.16	0.013
Error	10	1.41713E+14	1.41713E+13		
Lack-of-Fit	1	2.90885E+12	2.90885E+12	0.19	0.674
Pure Error	9	1.38804E+14	1.54227E+13		
Total	14	3.68953E+14			

Model Summary

S	R-sq	R-sq(adj)	R-sq(pred)
3764480	61.59%	46.23%	33.69%

Coefficients

Term	Coef	SE Coef	T-Value	P-Value	VIF
Constant	1753185	1254626	1.40	0.193	
Θ	3015035	1229737	2.45	0.034	478.43
L2	-91375866	32322770	-2.83	0.018	754.44
Θ*Θ	-38461	17245	-2.23	0.050	154.94
L2*L2	34162304	11285026	3.03	0.013	336.62

Regression Equation

P = 1753185 + 3015035 Θ - 91375866 L2 - 38461 Θ*Θ + 34162304 L2*L2

Fits and Diagnostics for Unusual Observations

Obs	P	Fit	Resid	Std Resid	
3	12629200	1753185	10876015	3.06	R

R Large residual

FIGURE 62. DOE procedure second try.

REFERENCES

REFERENCES

[1] Kirsten, C., 2017, “Winning in a More Dynamic and Inclusive Market,” Paint and Coating Industry, 33(7), p. 5.

[2] MarketsAndMarkets, 2017, “Automotive Adhesives Market by Resin Type (Polyurethane, Epoxy, Acrylic, Silicone, SMP, Polyamide), Application (Body-in-White, Paint Shop, Powertrain, Assembly), Vehicle Type (Buses, Trucks, LCV), and Region - Global Forecast to 2021,” accessed June 16, 2018, https://www.marketsandmarkets.com/Market-Reports/automotive-adhesive-market-36961165.html.

[3] Marz, S., and Ashby, D.M., 2000, “Sealing Challenges for The Medical Industry: Properly designed seals protect against dirt, dust, fluids, and EMI,” accessed June, 16, 2018, http://www.machinedesign.com/archive/sealing-challenges-medical-industry.

[4] Griffin, W., 1977, "Fundamentals of Noncuring Sealants for Aircraft Fuel Tanks," Air Force Materials Lab, Wright Air Force Base, OH.

[5] Giannis, S., Adams, R., Clark, L., and Taylor, M., 2008, “Peel Behaviour of Aircraft Fuel Tank Sealants: The Effect of Peel Angle, Sealant Layer Thickness and Peel Rate,” Journal of Adhesion Science and Technology, 22(13), pp. 1495-1522.

[6] Mandeville. D., 2008, “Selecting Application Process Technologies for Adhesive and Sealant Dispensing Applications,” Adhesives and Sealant Industry, 15(2), p. 4.

[7] Barnes, H. A., Townsend, P., and Walters, K., 1971, “On Pulsatile Flow of non-Newtonian Liquids,” Rheologica Acta, 10(4), pp. 517-527.

[8] Hyun, J., Wang, S., and Yang, S., 2014, “Topology Optimization of the Shear Thinning non-Newtonian Fluidic Systems for Minimizing Wall Shear Stress,” Computers & Mathematics with Applications, 67(5), pp.1154-1170.

[9] Ghiaasiaan, S. M., 2011, Convective Heat and Mass Transfer, 1st ed., Cambridge University Press, New York, NY.

[10] Soane, D.S., and Houston, M.R., 2003, “Method for Synthesizing Thermo-Expandable Polymeric Microspheres,” U.S. Patent 6617364 B2.

[11] Payri, R., Molina, S., Salvador, F. J., and Gimeno, J., 2004, “A Study of the Relation Between Nozzle Geometry, Internal Flow and Sprays Characteristics in Diesel Fuel Injection Systems,” KSME International Journal, 18(7), pp.1222-1235.

[12] PPG Industries “Nozzles,” accessed June, 10, 2018, http://www.ppgaerospace.com/ Products/ Packaging/Semco-Packaging-and-Application-Systems/Nozzles.aspx

[13] Hassine, M., 2012, Advanced Methods for Practical Applications in Fluid Mechanics, InTech., Tunisia, Chap. 10.

[14] Borrvall, T., and Petersson, J., 2003, "Topology Optimization for Fluid in Stokes Flow," International Journal for Numerical Methods in Fluids, 41(1), pp.77-107.

[15] Guest, J. K., and Prévost, J. H., 2006, "Topology Optimization of Creeping Fluid Flows Using a Darcy–Stokes Finite Element," International Journal for Numerical Methods in Engineering, 66(3), pp. 461-484.

[16] Nguyen, Q. H., Han, Y. M., Choi, S. B., and Wereley, N. M., 2007, " Geometry Optimization of MR Valves Constrained in a Specific Volume Using the Finite Element Method," Smart Materials and Structures, 16(6), pp. 2242-2252.

[17] Pingen, G., and Maute, K., 2010, "Optimal Design for non-Newtonian Flows Using a Topology Optimization Approach," Computers & Mathematics with Applications, 59(7), pp.2340-2350.

[18] Giannis, S., Adams, R. D., Clark, L. J., and Taylor, M. A., 2008, "The Use of a Modified Peel Specimen to Assess the Peel Resistance of Aircraft Fuel Tank Sealants," International Journal of Adhesion and Adhesives, 28(4-5), pp. 158-175.

[19] PPG Industries, "Aerospace Sealants Application Guide," accessed June, 10, 2018, http://www.ppgaerospace.com/Products/Sealants/Application-Guides.aspx.

[20] Yin, S., Meyer, M., Li, W., Liao, H., and Lupoi, R., 2016, "Gas Flow, Particle Acceleration, and Heat Transfer in Cold Spray: a Review," Journal of Thermal Spray Technology, 25(5), pp. 874-896.

[21] Bird, R. B., 1976, "Useful non-Newtonian Models," Annual Review of Fluid Mechanics, 8(1), pp. 13-34.

[22] Nguyen, Q. H., and Nguyen, N. D., 2012, Continuum Mechanics-Progress in Fundamentals and Engineering Applications, InTech., Croatia, Chap. 3.

[23] Eesa, M., and Barigou, M., 2008, "CFD Analysis of Viscous non-Newtonian Flow Under the Influence of a Superimposed Rotational Vibration," Computers & Fluids, 37(1), pp. 24-34.

[24] Zikanov, O., 2010, Essential Computational Fluid Dynamics, John Wiley & Sons, Hoboken, NJ.

[25] Kulkarni, P. R., Singh, S. N., and Seshadri, V., 2007, "Parametric Studies of Exhaust Smoke–Superstructure Interaction on a Naval Ship Using CFD," Computers & Fluids, 36(4), pp. 794-816.

[26] Carreau, P.J., 1972, “Rheological Equations From Molecular Network Theories", Journal of Rheology, 16(1), pp. 99-127.

[27] Myers, R. H., Montgomery, D. C., and Anderson-Cook, C. M., 2009, Response Surface Methodology: Process and Product Optimization Using Designed Experiments, 3rd ed., John Wiley & Sons, Hoboken, NJ.